Geochemistry, Geophysics, Geosystems®

AGU ADVANCING EARTH AND SPACE SCIENCES

RESEARCH ARTICLE
10.1029/2023GC011334

Improving the Accessibility and Efficiency of Proton Irradiations for $^4He/^3He$ Thermochronology

C. L. Colleps[1], P. A. van der Beek[1], J. Amalberti[1], A. Denker[2], M. M. Tremblay[3], M. Bernard[1], A. H. Dittwald[2], and J. Bundesmann[2]

[1]Institute of Geosciences, University of Potsdam, Potsdam, Germany, [2]Helmholtz-Zentrum Berlin für Materialien und Energie GmbH, Protonen für die Therapie, Berlin, Germany, [3]Department of Earth, Atmospheric, and Planetary Sciences, Purdue University, West Lafayette, IN, USA

Abstract Synthesizing uniform and high concentrations of ^3He within minerals via high-energy proton irradiation is paramount for $^4He/^3He$ thermochronology and helium diffusion kinetic studies. Proton irradiations of geological material have hitherto exclusively been routinely conducted at the Francis H. Burr Proton Therapy Center (FHB); we thus explored alternative irradiation protocols at two European-based facilities with the intention to improve the accessibility and efficiency in obtaining $^4He/^3He$ data. We conducted a single irradiation at the Paul Scherrer Institute (PSI) using an approach most similar to that used at FHB (wide, high-energy beam), and four irradiations at the Helmholtz Zentrum Berlin (HZB) using a newly developed in-vacuum irradiation protocol in a narrow, lower-energy but high-intensity beam. Internal shards of Durango apatite were irradiated in all experiments; $^4He/^3He$ release spectra and bulk ^3He concentrations of PSI and HZB-irradiated Durango shards were compared to those from FHB to assess the quality of each experiment in terms of the quantity and uniformity of synthesized ^3He. While ^3He was uniformly synthesized in PSI-irradiated Durango shards, the bulk ^3He concentration was below the required threshold due to limitations on the maximum allotted proton flux. Over the course of four irradiation experiments at HZB, the protocol evolved to ensure that uniform and high concentrations of ^3He can be consistently induced. Furthermore, we demonstrate how HZB irradiations can be replicated using computer simulations, permitting the use of simulations to inform future modifications of the irradiation protocol in order to optimize the uniformity of the ^3He distribution across all irradiated samples.

Key Points:

- $^4He/^3He$ Thermochronology requires the synthesis of uniform and high concentrations of ^3He within minerals via proton irradiation
- Durango apatite was irradiated at three proton irradiation facilities for quality assessment and comparison
- A new in-vacuum and high-intensity irradiation protocol was established that has potential to improve the throughput of $^4He/^3He$ analyses

Supporting Information:

Supporting Information may be found in the online version of this article.

Correspondence to:

C. L. Colleps,
colleps@uni-potsdam.de

Citation:

Colleps, C. L., van der Beek, P. A., Amalberti, J., Denker, A., Tremblay, M. M., Bernard, M., et al. (2024). Improving the accessibility and efficiency of proton irradiations for $^4He/^3He$ thermochronology. *Geochemistry, Geophysics, Geosystems*, *25*, e2023GC011334. https://doi.org/10.1029/2023GC011334

Received 6 NOV 2023
Accepted 22 JAN 2024

1. Introduction

The (U-Th)/He thermochronometric system is based on the thermally-activated diffusive loss of radiogenic ^4He atoms out of U- and Th-bearing accessory minerals (Farley, 2002; Reiners et al., 2002; Zeitler et al., 1987). Alpha particles are produced at known rates along U and Th decay chains, and a conventional (U-Th)/He date can be calculated following bulk mineral extraction and measurement of parent-daughter concentrations. The calculated date broadly reflects the timing when the analyzed mineral cooled below its respective closure temperature (Dodson, 1973), and thus thermochronometric dates are commonly used to extract thermal histories from rocks to infer periods of exhumation or burial. However, the thermal information obtained from a single conventional (U-Th)/He date is limited and will result in non-unique thermal histories that require additional data to resolve. One approach to augment the information extracted from a single crystal is to measure its diffusive-loss distribution of ^4He, which is highly dependent on the sample's thermal history (Shuster & Farley, 2004). Coupling a grain's ^4He diffusive distribution with its (U-Th)/He date significantly enhances the resolution of thermal histories extracted from a single grain, which is attainable with the advancement of $^4He/^3He$ thermochronology.

The $^4He/^3He$ method provides information about the spatial distribution of ^4He within a single crystal by comparing the ratio evolution of natural, non-uniform ^4He to synthetically induced, uniform ^3He via stepwise degassing analysis (Shuster & Farley, 2004; Shuster et al., 2004). The natural ^4He distribution is most commonly inferred from a sample's $^4He/^3He$ release spectrum, which plots the $^4He/^3He$ ratio from each heating step (normalized to the bulk sample $^4He/^3He$ ratio) as a function of the cumulative fraction of ^3He (ΣF_{3He}) degassed. Whereas recent experiments have revealed the potential of $^4He/^3He$ thermochronology applied to zircon (Brennan et al., 2020; Tripathy-Lang et al., 2015), this approach has most commonly been applied using apatite to extract low-temperature, high-resolution thermal histories capable of tracking detailed

histories of processes including glacial erosion (Shuster et al., 2005, 2011; Valla et al., 2011), canyon incision (Flowers & Farley, 2012), knick-point migration (Fechtig & Kalbitzer, 1966), and drainage reorganization (Tremblay et al., 2015). Furthermore, the ^{4}He/^{3}He method permits the extraction of grain-specific He diffusion kinetics based on the Arrhenius behavior of uniformly induced ^{3}He during stepped-heating experiments with precise temperature control (Shuster et al., 2006). The ability to directly constrain intrasample variability in He diffusivities from individual grains is imperative not only to assess and refine modern radiation damage accumulation and annealing models (Flowers et al., 2009; Gautheron et al., 2009; Guenthner et al., 2013; Shuster et al., 2006) but also to advance the utility of employing individual grains as their own unique thermochronometer independent of system-scale kinetics.

Despite the appeal of ^{4}He/^{3}He as a powerful thermochronometric tool, this technique has arguably remained underutilized since its initial development nearly 20 years ago (Shuster & Farley, 2004). More than ever, several laboratories across the globe are now equipped with sector-field noble gas mass spectrometers with ^{4}He/^{3}He measurement capabilities. However, the requirement to induce high concentrations of ^{3}He uniformly within individual crystals remains a major bottleneck hindering the production of ^{4}He/^{3}He thermochronologic data. Synthesizing high concentrations of ^{3}He uniformly within minerals requires their exposure to moderate- to high-energy protons at a particularly high fluence ($>1 \times 10^{15}$ protons/cm^2), during which ^{3}He is produced by nearly all targeted nuclei as a product of irradiation-induced spallation reactions (Shuster et al., 2004). Unfortunately, facilities with the capabilities and willingness to conduct such high-fluence proton-irradiation experiments are few and far between—the Francis H. Burr Proton Therapy Center (FHB) at Massachusetts General Hospital (Boston, MA) is currently the only facility world-wide that has routinely conducted these irradiations for the growing community. The growing demand for ^{4}He/^{3}He data and ^{3}He diffusion-focused studies will require improved irradiation accessibility and efficiency by establishing collaborations with other facilities and exploring new procedures.

Finding irradiation facilities that meet the archetype specifications for successful ^{4}He/^{3}He analysis is a challenge. Ideally, these specifications include (a) a broad, uniform, and high-energy proton beam (>1 cm diameter; >200 MeV); (b) a high proton flux ($>1 \times 10^{11}$ protons/cm^2/s); and (c) the time and willingness to conduct routine experiments. A broad, uniform proton beam promotes a uniform radial production of ^{3}He, whereas a high-energy beam permits the irradiation of multiple samples at once along a thick sample stack while ensuring sufficient activation across the entire target. Based on ^{3}He production cross sections from Mg, Al, and Si, spallation ^{3}He production significantly drops off below ~30 MeV and appears at first order to plateau with only a modest increase at energies above ~50–70 MeV, but existing data between this energy range are sparse (Leya et al., 1998). A high proton flux (or intensity) ensures that the minimum required fluence of 1×10^{15} protons/cm^2 may be reached within a timely manner (~1–10 hr). Facilities must be willing to conduct such irradiations routinely; the majority of facilities meeting the high-energy and high-flux specificities are proton therapy centers dedicated to clinical practice and medical research, and thus not directly geared toward establishing routine irradiations of geologic material. Furthermore, institution-specific regulations may place thresholds on maximum permitted fluxes, beam energies, and/or annual-fluence budgets, often deeming many facilities unsuitable for the ^{4}He/^{3}He requirements. Finally, radiation safety must be taken into consideration, and samples are typically subjected to prolonged post-irradiation cool-down periods that may be improved upon.

In this contribution, we review the current state-of-the-art proton irradiation procedures for geological materials. Using samples irradiated at FHB as a control, we present results from irradiation experiments conducted at two new prospective facilities using a "conventional" irradiation approach and a newly developed protocol. We assess the advantages and disadvantages of each protocol in view of (a) bulk ^{3}He concentrations synthesized, (b) uniformity of ^{3}He induced, and (c) overall efficiency in terms of both duration of irradiation and time from irradiation to ^{4}He/^{3}He measurements. In addition, we utilize computer simulations to compare modeled ^{3}He fluxes across the sample assemblies to measured data, and we discuss how such simulations may be used to inform future irradiation experiments. We lastly discuss the future outlook of proton irradiations for ^{4}He/^{3}He thermochronology as well as alternative approaches for ^{3}He synthesis in natural materials.

2. Background and Motivation: Proton Irradiations

The first proton irradiation dedicated toward ^{4}He/^{3}He analysis was conducted at the Harvard Cyclotron Lab, and involved the exposure of samples contained within a 22 mm-thick stack of seven individual lucite discs with a diameter of 15 mm. The sample assembly was exposed to a ~4.0 nA, 147 MeV proton beam for ~10 hr for a total

fluence of $\sim 10^{14}$ protons/cm^2 (Shuster et al., 2004). Each disc hosted 3–7 sample pits containing multiple milligrams of mineral separates from various samples, including internal shards of gem-quality Durango apatite. Internal shards of Durango apatite have been extensively utilized to calibrate ^{4}He diffusivities within pristine apatite—the ^{4}He distribution within those shards is expected to be uniform, as internal shards of these volcanic apatites have not experienced alpha-ejection or diffusive loss. Internal shards of Durango apatite are thus an ideal matrix-matched material to assess the uniformity of ^{3}He synthetized during proton bombardment. If spallation ^{3}He is uniformly induced within a Durango sample, its ^{4}He/^{3}He release spectrum following stepped-heat analysis should be flat with a constant ratio of 1.00 under the assumption that the diffusivities for ^{4}He and ^{3}He are equivalent (Shuster et al., 2004).

Results from the initial irradiation at the Harvard Cyclotron Lab indicate that exposing samples to a fluence of $\sim 5.2 \times 10^{14}$ protons/cm^2 produces $\sim 2.0 \times 10^8$ atoms/mg of spallation ^{3}He in Durango apatite, corresponding to $\sim 10^6$ atoms of ^{3}He within a single ~160–180 μm shard (Shuster et al., 2004). In order to ensure that the ^{3}He outgassed at each heating step was sufficiently above ^{3}He detection limits for accurate measurements, initial ^{4}He/^{3}He stepped-heating experiments from this study were conducted using multi-grain aliquots. Initial diffusion experiments on a multi-grain aliquot of irradiated Durango shards indicated that ^{3}He and ^{4}He have similar kinetic behavior, and the resulting flat ^{4}He/^{3}He release spectrum confirmed a uniform distribution of spallation ^{3}He. The ^{4}He/^{3}He ratios from this experiment remained consistent until the last five measurements ($\Sigma F^{3He} > 0.96$), where a decreasing rollover of ^{4}He/^{3}He ratios was observed, potentially indicating a slightly faster ^{4}He diffusivity (D) to that of ^{3}He ($D^{4He}/D^{3He} = 1.03$) (Shuster et al., 2004).

Analyzing multiple grain aliquots for non-standard apatites with unknown thermal histories has the potential to result in erroneous ^{4}He/^{3}He release spectra due to intrasample variability in single-grain He diffusivities induced by radiation damage (Farley et al., 2010). It is thus preferred to analyze individual crystals for ^{4}He/^{3}He release spectra. However, analyzing a crystal with an equivalent spherical radius (ESR) greater than ~60 μm requires a minimum concentration of $\sim 10^9$ atoms/mg of spallation ^{3}He. At this concentration, degassing ~1%–5% of the grain equates to measuring ^{3}He on the order of 10^4 atoms, sufficiently above the typical ^{3}He blank detection limit of our mass spectrometer on the order of 10^3 atoms. Accordingly, irradiations subsequently conducted at FHB evolved to routinely achieve fluences of 10^{15}–10^{16} protons/cm^2 within ~5–9 hr of proton bombardment to ensure sufficient ^{3}He is produced for single-grain analysis (Cuffey et al., 2022; Dai et al., 2021; Fox et al., 2014). In addition, the sample assembly for the FHB irradiations has evolved into a target of multiple cylindrical HDPE capsules axially stacked within quartz tubes (Figure 1a). Each HDPE capsule includes milligrams of mineral separated from an individual sample tightly packed within an Al foil packet, which is intended to promote balancing of ejected ^{3}He within a grain with implanted ^{3}He sourced from closely clustered adjacent grains or the foil packet (Schaeffer et al., 1966; Shuster et al., 2004).

To date, all published samples analyzed for ^{4}He/^{3}He analysis have been irradiated using the procedures described above. Whereas this procedure has resulted in reliable and reproducible ^{4}He/^{3}He data sets, many of the complexities and assumptions involved in proton irradiations to induce uniform spallation ^{3}He within individual crystals have remained largely undiscussed in the community. Only recently have researchers alluded to potential irradiation-induced edge-effects (Cuffey et al., 2022) and inhomogeneous ^{3}He production via mm-scale proton fluence gradients (Vermeesch et al., 2023) that may affect ^{4}He/^{3}He data. Without further insight into the quality control of irradiations through the routine analysis of standards placed at numerous lateral and radial locations along the irradiated target, it remains difficult to directly assess these potential problems.

This study was primarily motivated by the desire to increase the accessibility of ^{4}He/^{3}He thermochronology through establishing a new facility for routine proton irradiations. During the course of this study, our motivation evolved to focus on many of the logistical and experimental complexities involved in inducing uniform spallation ^{3}He in geological materials. We conducted irradiation experiments—primarily irradiating shards of Durango apatite—at two new prospective particle accelerator facilities: the Paul Scherrer Institute (PSI) in Villigen, Switzerland, and the Helmholtz Zentrum Berlin (HZB) in Berlin-Wannsee, Germany. The goal following these irradiations was to evaluate the potential of each procedure to consistently reproduce ^{4}He/^{3}He release spectra of FHB-irradiated Durango shards with sufficient spallation ^{3}He concentrations.

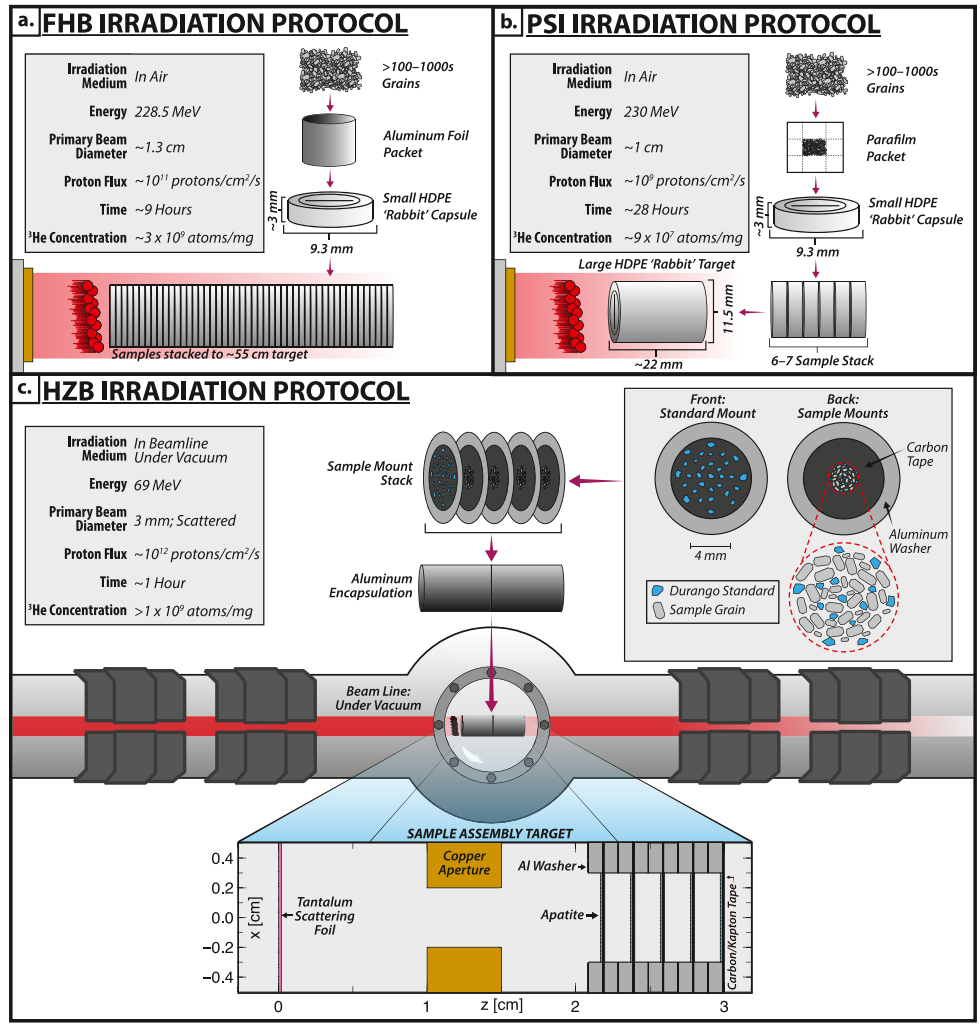

Figure 1. *Schematic representation of the sample preparation and parameters applied to proton irradiations conducted at* (a) *the Francis H. Burr Proton Therapy Center (FHB)*, (b) *the Paul Scherrer Institute (PSI)*, *and* (c) *Helmholtz Zentrum Berlin* (*HZB*). To prevent excessive in-air activation during the high-intensity irradiations at HZB, samples were placed directly within the beam-line under high-vacuum.

3. Methods

3.1. Facility Selection

We explored the feasibility of conducting high-fluence proton irradiations at varying prospective facilities within Europe—ideally those with a broad, high-energy and high flux proton beam. Facilities offering near-identical specifications to those at FHB were most-often dedicated to medical treatment and research, and thus irradiations for the $^{4}He/^{3}He$ method were generally not permitted (at least for continuing routine experiments). Accordingly, we relaxed some ideal specification thresholds during the search for plausible facilities, which was accommodated with the requirement to development and assess "non-conventional" protocols. Durango apatite shards were included in an irradiation conducted at FHB, and we consider that these shards serve as a control to assess the quality of irradiations conducted at PSI and HZB. We also consider the protocol at FHB as a "conventional" procedure. A single irradiation experiment was conducted at PSI involving the irradiation of a marginally modified conventional sample target assembly, whereas 4 irradiation experiments were conducted at HZB using a "non-conventional," in-vacuum irradiation protocol described in detail (Figure 1).

3.1.1. Francis H. Burr Proton Therapy Center

An irradiation was conducted at FHB in March 2022. Included in this irradiation were several milligrams of Durango apatite shards, which were first tightly contained within aluminum foil capsules and subsequently placed in HDPE cylindrical capsules with a diameter of ∼9 mm and height of ∼3 mm. Several HDPE capsules were stacked to a length of ∼555 mm for irradiation, and the Durango shards used in this study were located between ∼100 and 140 mm from one end of the stack. The target was exposed to a ∼13 mm diameter 229 MeV proton beam for a total of ∼9 hr with an intensity of $\sim 10^{11}$ protons/cm^2/s (Figure 1a). The target received a total fluence of 9.98×10^{15} protons/cm^2, and was rotated 180° halfway through the irradiation to ensure the target received a symmetrical axial exposure. Following the irradiation, the target was held at FHB for ∼2.5 months until it was shipped to Purdue University in June 2022, after which it was properly stored for an additional month to ensure safe extraction of the samples.

3.1.2. Paul Scherrer Institute Irradiation

An irradiation experiment was conducted at PSI in July 2021 following a protocol most similar to that used for FHB irradiations; however, the maximum flux at PSI was orders of magnitude lower due to safety regulations that limit the maximum beam current to 2 nA for energies >200 MeV, restricting the proton intensity. Several milligrams of apatite were tightly packed into Parafilm® packets, which were then placed and centered inside individual HDPE capsules (Figure 1b). Parafilm® packets were used as replacements of Al foil packets at the request of PSI in order to homogenize the material compositions irradiated and to limit the activation of Al foils. A total of five HDPE sample capsules were stacked within a larger, ∼22 mm long HDPE capsule, which served as the irradiation test target. Multiple internal shards (>100 ranging between ∼200 and 400 μm in size) of Durango apatite were loaded into two of the five capsules, which were arranged both at the front and back of the sample stack. The sample target was exposed to a uniform 2 nA proton beam with a diameter of ∼1 cm, energy of 230 MeV, and flux of $\sim 2 \times 10^9$ protons/cm^2/s. Following a total irradiation time of ∼27.9 hr, the sample target received a total fluence of $\sim 2.0 \times 10^{14}$ protons/cm^2—similar to that achieved in the initial irradiations of Shuster et al. (2004). Although the resulting fluence is less than the 10^{15} protons/cm^2 minimum requirement to analyze typical natural samples with an ESR > 60 μm, the Durango shards irradiated here were large enough to release sufficient ^{3}He above blank detection limits for reliable ^{4}He/^{3}He measurements. We thus consider that the ^{4}He/^{3}He results presented here from the PSI irradiation are most representative of the modern FHB protocol in terms of the uniformity of spallation ^{3}He but with a significantly lower ^{3}He concentration.

3.1.3. Helmholtz Zentrum Berlin Irradiations

The HZB cyclotron sources a primary ∼3 mm full width half maximum (FWHM) proton beam with an energy of ∼68 MeV at permissible intensities ranging from $\sim 10^4$–10^{13} protons/cm^2/s. Whereas the comparatively narrower proton beam will induce a higher intensity for a given current, beam intensities can be further maximized by placing samples directly in the beam line and under vacuum (Figure 1c). The fully enclosed, in-vacuum irradiation furthermore provides a safe means to reach the high proton fluences required for ^{4}He/^{3}He analysis. Accordingly, we conducted a series of in-vacuum proton irradiation experiments at HZB, requiring a notably modified protocol and sample assembly.

Since September 2021, a total of four in-vacuum proton irradiations were conducted at HZB (HZB1, HZB2, HZB3, and HZB4) using Durango shards mounted at multiple positions for quality assessment. The sample assembly for in-vacuum irradiations consisted of a stack of 4–6 samples mounted on carbon tape attached to ∼1 mm thick metal washers (pure aluminum or stainless steel) with an outer diameter of 12 mm. Individual apatite crystals or standard shards were typically mounted radially on the carbon tape in a single layer and within a ∼2 mm radius (Figure 1c). Each sample mount was stacked and contained within a customized spring-loaded aluminum tube, which was mounted onto a motorized track that moved the sample into and out of the beam line under high vacuum. The motorized track assembly additionally contained a series of copper apertures and scintillator foils, which were moved into the beamline to evaluate, assist, and control both beam alignment and geometry. Each irradiation experiment involved minor differences in parameters and/or sample geometries that were informed from both previous irradiation results and computer simulations. The results of each experiment along with details regarding protocol modifications are provided in Section 4.3.

3.2. Bulk ^{3}He and ^{4}He/^{3}He Measurements

Irradiated Durango shards from each irradiation were picked, and the mass of each individual shard was measured using a microbalance (repeatability of ±0.001 mg). For HZB irradiated Durango, the radial location of each selected shard was mapped out. Following mass measurement, each Durango shard was morphometrically measured, photographed, and packed within Pt packets. Each Pt packet was placed into a sample chamber with a sapphire viewport connected to a gas preparation line, which was pumped down to ultra-high vacuum ($\sim 10^{-9}$ Torr) after sample loading. Grains from initial irradiation experiments (PSI, HZB1, and HZB2) were first measured for bulk ^{4}He and ^{3}He concentrations by direct heating with a 75 W diode laser to a temperature >900°C for 5 min, followed by an identical re-extraction heating step to ensure all He was degassed from the sample. Durango shards from subsequent irradiations were analyzed via a series of stepped-heating analyses to evaluate each grain's ^{4}He/^{3}He release spectrum for uniformity of spallation ^{3}He. Grains were gradually heated and degassed at a range of heating steps (~7–30 heating steps) to efficiently evaluate the quality of the irradiation across the sample assembly, and efforts were made to attempt to probe each grain's edge at a higher resolution for ^{4}He/^{3}He ratios. At the time of our initial step-heating analysis on PSI and HZB3 irradiated Durango shards, aliquots were loaded into a multi-sample planchette with 36 positions, and individual Pt packets were primarily heated using a defocused 0.5–1.0 mm laser spot. At the time of these analyses, the minimum temperature sensitivity of the pyrometer equipped with the diode laser was 300°C; therefore, initial heating steps were achieved by incrementally increasing the laser power at each step. Once the pyrometer began reading temperatures >300°C, these readings were used as a relative measure to ensure each step was heated more than the previous step—we note that the primary intent of these experiments did not require temperature precision. Direct, defocused, and power-controlled laser heating of the Pt packets, however, proved sensitive to overheating (e.g., Brennan et al., 2020), which resulted in inconsistencies in probing each grain' edge at low-temperature steps. To account for these inconsistencies, an indirect laser-heating protocol was developed using a custom-made alumina crucible coupled with a K-type thermocouple to improve relative temperature control (Amalberti et al., 2023), and this procedure was utilized during stepped-heating analyses of HZB4 and FHB-irradiated Durango shards.

The gas released from each step was expanded into a sample-gas preparation line equipped with a cryogenic trap for the purification and concentration of ^{4}He and ^{3}He. Purified gas was released from the cryotrap at 50 K and inlet into a Thermo Helix Split Flight Tube mass spectrometer, and ^{4}He and ^{3}He masses were measured simultaneously with a Faraday cup and a CDD electron multiplier, respectively. Air standards and helium blanks were analyzed every 5–6 unknown measurements, and each unknown ^{4}He/^{3}He measurement was blank corrected.

Bulk ^{3}He concentrations (atoms/mg) and ^{4}He/^{3}He release spectra were used to assess the quality of each irradiation with regard to inducing uniform spallation ^{3}He at sufficient concentrations. A constant normalized ^{4}He/^{3}He ratio of 1.00 ± 0.05 measured from each heating step of a Durango shard indicates that ^{3}He was uniformly synthesized. In contrast, variable ^{4}He/^{3}He release spectra would indicate inhomogeneities in the synthesis of spallation ^{3}He. Durango ^{4}He/^{3}He release spectra revealing individual measurements with normalized ^{4}He/^{3}He ratios >1 would reflect regions within the shard with a relative depletion of ^{3}He, whereas normalized ^{4}He/^{3}He ratios <1 would indicate regions with a relative enrichment of ^{3}He.

3.3. Computer Simulations: Particle and Heavy Ion Transport Code System

An advantage to the in-vacuum irradiations at HZB is that the sample assembly geometry is comparatively simple (Figure 1c) due to the use of limited materials arranged in clearly defined axial layers (including apatite samples). The well-defined geometries employed in the HZB irradiations provide a unique opportunity to compare observed patterns in the induced spallation ^{3}He distribution with computer-simulated predictions. Accordingly, we used the Particle and Heavy Ion Transport code System (PHITS) (Iwamoto et al., 2022; Sato et al., 2018) to simulate the spatial distribution of the proton, ^{3}He, and ^{4}He fluxes across a defined 3D configuration that incorporates the compositions and geometries of the true sample assembly. PHITS is a Monte Carlo particle transport code that simulates the transport and collision of nearly all particles over a wide range of energy up to 1 TeV, using multiple nuclear-reaction models and data libraries (Sato et al., 2018). The event generator mode incorporated into PHITS additionally permits accounting for secondary particles produced in cascade reactions induced by the primary incident particle, and so He particles generated by secondary reactions are also tallied in the simulations. Furthermore, in accounting for secondary particles produced in nuclear reactions, PHITS permits a more realistic

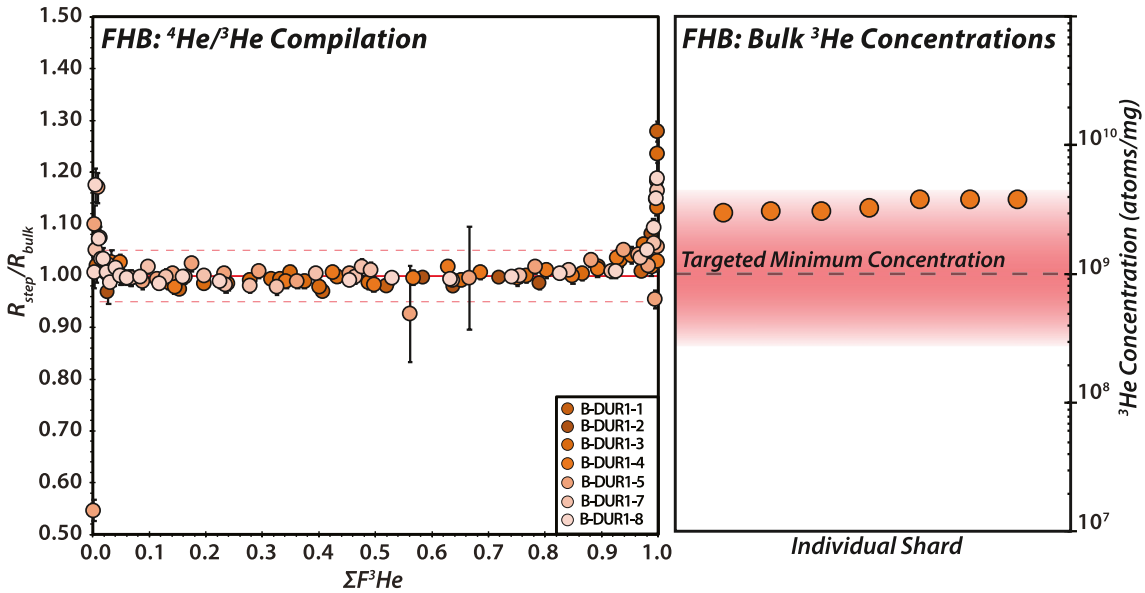

Figure 2. *Compilation of $^4He/^3He$ release spectra and bulk spallation ^3He concentrations from individual Durango apatite shards irradiated at the Francis H. Burr Proton Therapy Center (FHB).* In the $^4He/^3He$ plot, the *y*-axis is defined by the $^4He/^3He$ ratio analyzed at each heating step (R_{step}) normalized to the grain's bulk $^4He/^3He$ ratio (R_{bulk}), and the *x*-axis shows the cumulative fraction of ^3He degassed (ΣF_{3He}). The general ^3He uniformity induced within Durango shards at high concentrations at FHB is evident in the comparatively uniform $^4He/^3He$ release spectra, and these spectra serve as a means of comparison when assessing alternative proton irradiation facilities and protocols.

relative assessment of displacements per atom (DPA; i.e., radiation damage) within a given material when exposed to different incident particles at different energies (e.g., Iwamoto et al., 2012).

Simulations were conducted in PHITS using parameters and geometries that most closely matched those applied for different HZB irradiations, and further simulations were run adjusting parameters such as proton beam diameter, beam energy, the sample mount spacing, apatite thickness, and mount compositions to assess their influence on the ^3He flux. Whereas most Durango shards mounted and analyzed were block-shaped with widths of ~300–400 μm, the perpendicular axial and radial ^3He distributions were evaluated on the basis of an apatite thickness of 300 μm at radial positions defined by concentric rings with a width of 400 μm. The two perpendicular "rim-to-rim" axial and radial ^3He distributions simulated across each apatite layer (reflecting an individual Durango shard) were extracted, averaged, and to converted into an averaged "rim-to-core" ^3He distribution; we assume that this "rim-to-core" distribution appropriately estimates the three-dimensional ^3He distribution of the simulated apatite. By comparing the simulated "rim-to-core" ^3He distribution to an assumed uniform ^4He distribution, $^4He/^3He$ release spectra were modeled for "synthetic" Durango apatite shards at different axial and radial positions along the sample stack. Simulated $^4He/^3He$ release spectra were compared to those observed from HZB irradiated Durango shards, and simulation parameters were adjusted accordingly in attempts to optimize the uniformity of the ^3He distribution across the entire sample assembly.

4. Results

4.1. FHB Irradiations

A total of 7 Durango shards (B_DUR1) from FHB were analyzed for both coarse and high-resolution $^4He/^3He$ stepped-heating measurements. Bulk ^3He concentrations from these shards range from 2.9 to 3.5×10^9 atoms/mg with an average of 3.2×10^9 atoms/mg (Figure 2). Bulk ^4He concentrations ranged from 4.3 to 5.6×10^{12} atoms/mg with an average concentration of 4.8×10^{12} atoms/mg. As a whole, $^4He/^3He$ release spectra of each shard consistently revealed near-uniform and constant normalized $^4He/^3He$ ratios of 1.00 ± 0.05 throughout the degassing experiment with minimal deviations from shard-to-shard (Figure 2). However, $^4He/^3He$ ratios $\Sigma F_{3He} < 0.02$ were notably sporadic compared to the bulk ratios when the rim was probed at sufficient resolution. In addition, four of the seven shards revealed a systematic increase in $^4He/^3He$ ratios at $\Sigma F_{3He} > 0.97$, which we only observed when the $\Sigma F_{3He} > 0.90$ ratios were probed at higher resolutions (Figure S1 in Supporting

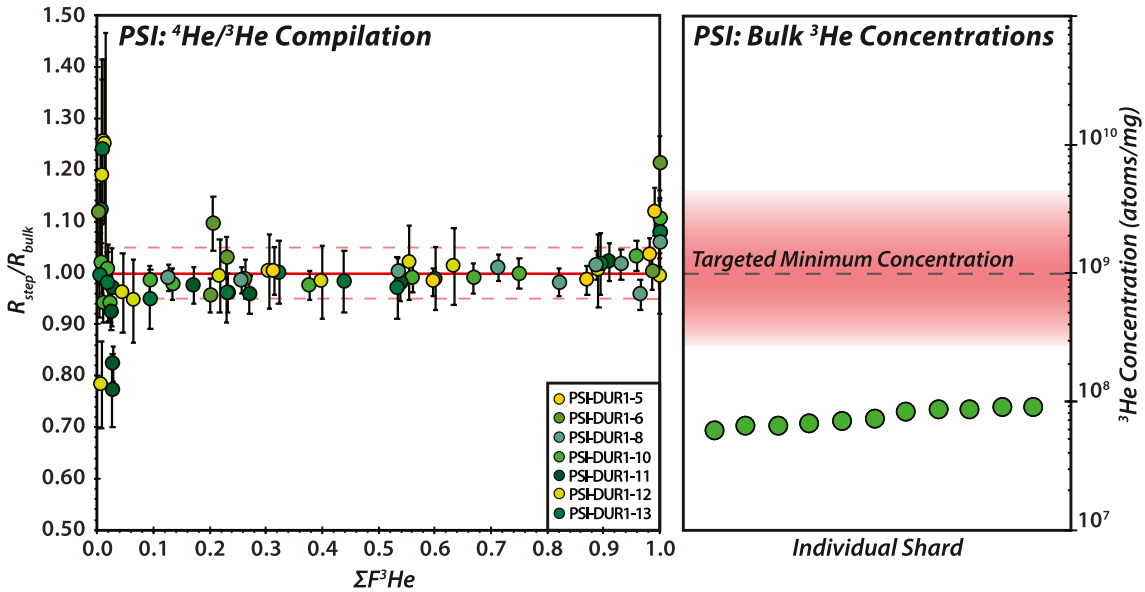

Figure 3. *Compilation of $^4He/^3He$ release spectra and bulk spallation ^3He concentrations from individual Durango apatite shards irradiated at the Paul Scherrer Institute (PSI).* While $^4He/^3He$ release spectra from PSI-irradiated Durango shards are comparable to those from *Francis H. Burr Proton Therapy Center*, the targeted ^3He concentration was not met after 28-hr irradiation due to a limit on the maximum proton flux. The low ^3He concentration also resulted in larger uncertainties in the $^4He/^3He$ ratios.

Information S1). Due to an analytical issue that occurred at two temperature steps in B-DUR1-5, the ^4He and ^3He signals were estimated from peak-centering values, and a 20% error was applied to these points.

4.2. PSI Irradiations

A total of four irradiated PSI Durango (PSI-DUR1) shards were analyzed for bulk ^3He and ^4He concentrations, and seven shards were analyzed for coarse $^4He/^3He$ stepped-heating measurements (Figure S2 in Supporting Information S1). Bulk ^3He concentrations from all 11 shards ranged from 5.8 to 8.9 $\times$ 10^7 atoms/mg with an average of 7.5 $\times$ 10^7 atoms/mg (Figure 3). Bulk ^4He concentrations ranged from 2.48 to 4.6 $\times$ 10^{12} atoms/mg with an average of 3.5 $\times$ 10^{12} atoms/mg. A compilation of coarse stepped heating $^4He/^3He$ measurements from seven shards consistently revealed near-uniform $^4He/^3He$ ratios with an error of 1.00 at $\Sigma F_{3He} > 0.10$. At $\Sigma F_{3He} < 0.10$, $^4He/^3He$ ratios varied between 0.82 and 1.12 with an average of 0.97 $\pm$ 0.13 (2 standard deviations) (Figure 2). At ΣF_{3He} between 0.10 and 0.98, $^4He/^3He$ ratios ranged between 0.96 and 1.10, with an average ratio of 1.00 $\pm$ 0.05. At $\Sigma F_{3He} > 0.97$, $^4He/^3He$ ratios systematically increased until each shard was fully depleted of both ^3He and ^4He. Only one shard (PSI-DUR1-6) revealed an anomalous $^4He/^3He$ release spectrum compared to the general compiled trend, exhibiting highly variable $^4He/^3He$ ratios at $\Sigma F_{3He} > 0.25$.

4.3. HZB Irradiations

4.3.1. HZB1 Irradiation

The first irradiation conducted in September 2021 at HZB was primarily intended to evaluate if a proton beam energy of 68 MeV was sufficient to thoroughly activate apatite for the production of spallation ^3He. This is particularly important, as all previous $^4He/^3He$ irradiations were conducted at energies >150 MeV, and the activation cross-sections of Leya et al. (1998) are only suggestive of a plateau in total activation within the 50–70 MeV range. This irradiation additionally served as a means to test the in-vacuum beam alignment protocol for centering the beam directly on the sample. A single carbon-tape sample mount including ~300–500 μm shards of Durango apatite mounted within a 3 mm diameter was irradiated for 916 s with a 22 nA, 3 mm FWHM proton beam at an approximated peak intensity of 1 $\times$ 10^{12} protons/cm^2/s. Following the irradiation, the sample was safe to handle by October 2021 (i.e., 1 month after irradiation), after which eight individual Durango shards were selected for bulk-degassing ^3He and ^4He measurements.

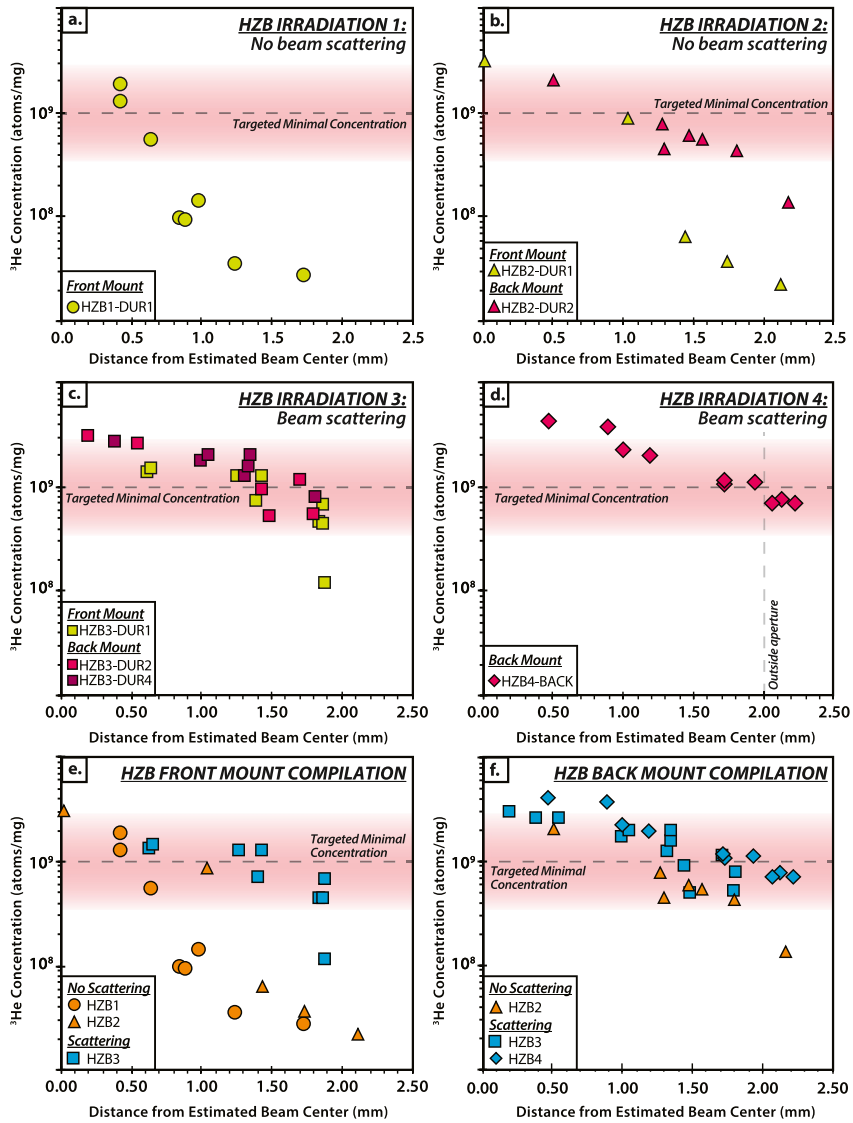

Figure 4. *Comparison of the radial ^{3}He yield induced in Durango apatite for each Helmholtz Zentrum Berlin (HZB) irradiation experiment*. Samples were directly exposed to the primary proton beam in HZB1 and HZB2 irradiations (a, b), whereas a tantalum foil was implemented in HZB3 and HZB4 irradiations (c, e) to scatter the primary proton beam and lessen the radial ^{3}He concentration gradient (e, f).

Bulk ^{3}He concentrations ranged from 2.7×10^{7} to 1.8×10^{9} atoms/mg with a distinctive radial distribution (Figure 4a), indicating that a beam energy 69 MeV is sufficient to generate spallation ^{3}He in apatite. Bulk ^{4}He concentrations ranged between 2.9×10^{12} and 4.1×10^{12} atoms/mg with an average of 3.5×10^{12} atoms/mg. The highest ^{3}He concentrations were observed in shards focused within a ~1-mm ring within the eastern-central portion of the mount (Figure S3 in Supporting Information S1). Outside this ring, bulk ^{3}He concentrations dropped below 1.0×10^{8} atoms/mg and further decreased to the western portion of the mount (Figure 4a). Considering that the radial distribution of ^{3}He most directly reflects the proton-intensity distribution, these initial results indicate that (a) the beam was off-center of the target and (b) the narrow beam intensity distribution imparts a potentially significant radial gradient in ^{3}He generation.

4.3.2. HZB2 Irradiation

A second irradiation was conducted in December 2021 with the motivations to (a) improve the in-vacuum beam centering, (b) assess radial differences in proton beam flux, and (c) assess if spallation ^{3}He is produced across a

thicker stack of six samples. The latter motivation is important to ensure that multiple samples may be irradiated at once—energy decreases down the sample assembly as the proton beam interacts with solid material. The cumulative thickness of the targeted apatite and carbon tape across the assembly is <3 mm (not including void between samples). Based on a conservative estimate using a simple linear stopping power of ∼2.5 MeV/mm for a 68 MeV beam in apatite (Ziegler et al., 2010), the sample farthest down-beam is expected to be exposed to a beam energy no less than ∼60 MeV. Six samples were mounted and stacked, including two Durango mounts which were placed both at the front and back sample positions. The sample assembly was irradiated for 1,200 s with a 3 mm FWHM beam at 22 nA with a similar estimated peak intensity of $\sim 1 \times 10^{12}$ protons/cm^2/s as in the first experiment. Following the irradiations, samples were safe to handle in January 2022, and seven Durango shards were selected from both the top (HZB2-DUR1) and bottom (HZB2-DUR3) mounts for bulk ^{3}He and ^{4}He measurements.

Bulk ^{3}He concentrations from HZB2-DUR1 shards (top mount) ranged from 1.8×10^7 to 3.1×10^9 atoms/mg (Figure 4b), and ^{4}He concentrations ranged from 2.8–3.6 $\times 10^{12}$ atoms/mg with an average of 3.3×10^{12} atoms/mg. Bulk ^{3}He concentrations from HZB2-DUR3 shards (bottom mount) ranged from 1.4×10^8 to 2.0×10^9 atoms/mg, and ^{4}He concentrations ranged from 3.0 to 4.3 $\times 10^{12}$ atoms/mg with an average of 3.6×10^{12} atoms/mg. On both the top and bottom mounts, the shard with the highest ^{3}He concentration was located on the westernmost, center location on the mount—likely indicative of the proton beam center (Figure S3 in Supporting Information S1). While the location of the highest ^{3}He concentration is similar between the top and the bottom mounts, the ^{3}He gradient significantly differs between the two (Figure 4b). The eastward ^{3}He gradient from the top mount drops down rapidly to $\sim 10^7$ atoms/mg ∼1.5 mm away from the shard with the highest ^{3}He concentration (HZB2-DUR1-4). In contrast, the ^{3}He gradient from the back Durango mount is notably gentler with the lowest ^{3}He concentration of 1.4×10^8 atoms/mg (HZB2-DUR2-4) located ∼2.2 mm east of the proposed beam center (Figure 4b).

The observed concentrations of spallation ^{3}He generated in individual shards were generally greater in the back sample mount, with a comparatively more uniform radial ^{3}He concentration distribution, than in the front mount (Figure 4b). This distinct difference in ^{3}He concentrations and radial distribution was most likely the result of (a) proton beam scattering after contact with the first mount and/or (b) the implantation of ^{3}He in back samples sourced from the up-beam sample mount(s). Assessing this behavior required further insight into the axial distribution of spallation ^{3}He generated across the sample assembly.

4.3.3. HZB3 Irradiation

A third irradiation was conducted at HZB in March 2022 with the motivation to (a) improve the uniformity of the radial proton flux, (b) examine both the radial and axial ^{3}He flux across the assembly, and (c) further improve the beam-centering protocol. To improve beam-centering, the motor-control on the in-vacuum assembly track was modified so that precise microadjustments could be made to ensure that the sample assembly was placed in precisely the same axial position as the calibration apertures used to maximize beam intensities and control beam geometry. A modified sample holder was introduced to include (a) a 200 μm-thick tantalum foil placed ∼3 cm up-beam from the front sample, with the intent of scattering the primary proton beam and (b) a 4 mm aperture was placed behind the scattering foil to assist with beam alignment. Four samples were stacked with a spacing of ∼1 mm, including three samples of Durango shards placed in the first (front), second, and fourth (back) positions. Due to an expected loss of intensity with the inclusion of the scattering foil, samples were exposed to a scattered proton beam with a higher 42 nA source current for 3,600 s. The scattering of the beam resulted in significant activation of the stainless-steel washers on each sample mount, and their removal from the carbon tape was required before the samples could be safely retrieved and transported. Irradiated samples were retrieved in May 2022, and Durango shards from all three sample positions were selected for coarse ^{4}He/^{3}He stepped heating experiments.

The bulk ^{3}He concentration of 9 individual shards from the front Durango mount (HZB3-DUR1) ranged from 1.2×10^8 to 1.4×10^9 atoms/mg with bulk ^{4}He concentrations ranging from 3.3 to 5.0 $\times 10^{12}$ atoms/mg (4.2 $\times 10^{12}$ atoms/mg average). Bulk ^{3}He measurements from 6 individual shards on the second Durango mount (located in the second position; HZB3-DUR2) ranged from 5.0×10^8–3.0×10^9 atoms/mg, and ^{4}He concentrations ranged from 2.5 to 4.9 $\times 10^{12}$ atoms/mg, with an average of 3.7×10^{12} atoms/mg. From the back Durango

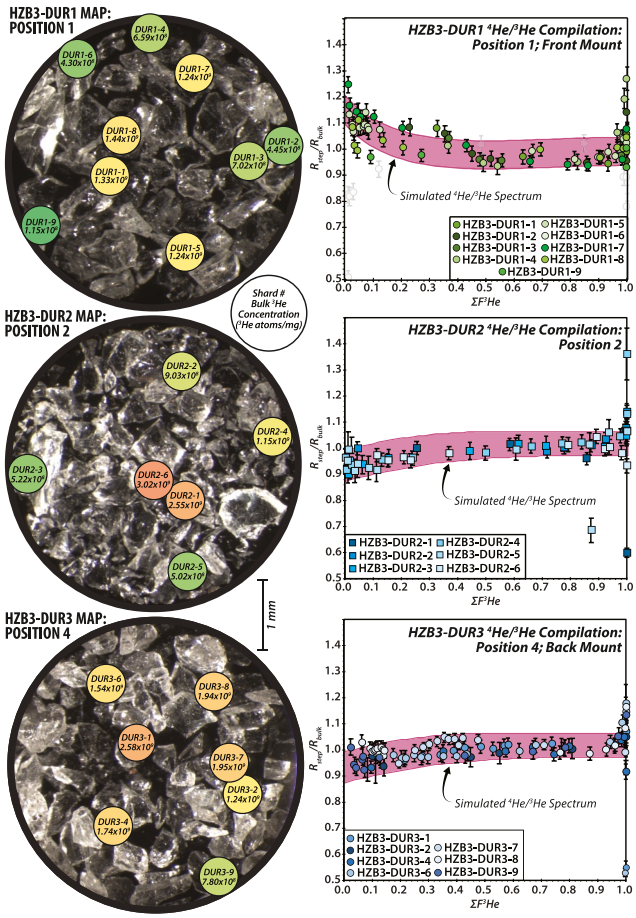

Figure 5. *Summary of the third Helmholtz Zentrum Berlin (HZB3) irradiation experiment with ^{3}He concentration maps of Durango apatite mounts at different axial positions (left column) and a compilation of single-shard ^{4}He/^{3}He release spectra obtained from each position (right column).* Durango shards from the front mount (position 1) systematically reveal a relative depletion of ^{3}He at $\Sigma F_{^3He} < 0.2$, whereas shards in each subsequent down-beam mount show a systematic enrichment of ^{3}He at $\Sigma F_{^3He} < 0.2$. The purple boundaries indicate the averaged simulated ^{4}He/^{3}He release spectra (±5% range) for each sample mount position (derived from simulations in Figures 8 and 9).

mount (HZB3-DUR3), bulk ^{3}He concentrations from seven shards ranged from 7.8×10^8 to 2.6×10^9 atoms/mg with ^{4}He measurements ranging from 3.6 to 4.6×10^{12} atoms/mg (4.2×10^{12} atoms/mg average) (Figure 4c).

Based on a cumulative overlay of ^{3}He concentrations from all three Durango mounts, the highest ^{3}He concentration observed was from a shard in the center of the second Durango mount (grain HZB-DUR2-6) (Figure 5). From this central location on all mounts, the radial ^{3}He concentration gradient gradually decreases—indicative of a successful beam centering. Compared to the previous two HZB irradiations, the radial gradient of the ^{3}He concentration distribution in the front sample (first contact with proton beam) was notably broader, with near-uniform ^{3}He concentrations between ~1.2 and 1.4×10^9 atoms/mg achieved within a ~1.25 mm radius (Figure 4e). A similar ^{3}He concentration gradient was observed in the HZB3-DUR2 and HZB3-DUR3 mounts, with individual shards generally yielding marginally higher ^{3}He concentrations within a given radial position when compared to HZB3-DUR1 (front mount).

The ^{3}He flux across the sample assembly was assessed by comparing the step-heating ^{4}He/^{3}He release spectra from individual Durango shards at different radial and axial positions. From the front Durango mount (HZB3-DUR1) (Figure S4 in Supporting Information S1), ^{4}He/^{3}He release spectra from 9 of the 11 shards show relative depletion of ^{3}He at $\Sigma F_{^3He} < 0.40$, where ^{4}He/^{3}He ratios systematically decrease from ~1.20 to ~0.95 (Figure 5). The ^{4}He/^{3}He release spectrum from $\Sigma F_{^3He} > 0.50$ generally remains consistent with ratios between 0.95 and 1.00 until the final degassing steps ($\Sigma F_{^3He} > 0.97$), where ratios typically exceed 1.00. One shard (HZB3-DUR1-9) with only 3-step coarse degassing showed relative ^{3}He uniformity throughout the ^{4}He/^{3}He, and was located at the southwestern most edge of the mount, recording the lowest ^{3}He concentration. Another single shard from the front Durango mount exhibited a ^{4}He/^{3}He release spectrum with ratios increasing from 0.80 to 1.00 at $\Sigma F_{^3He} < 0.20$, after which the ratios remained relatively consistent at 1.00 until falling below 1.00 at $\Sigma F_{^3He} > 0.97$. Whereas this release spectrum indicates an enrichment of ^{3}He at the rim, we note that this shard was partially mounted beneath a larger shard during the irradiation. Accordingly, we suspect that the implantation of ^{3}He sourced from the overriding shard may explain this anomalous release spectrum from the front Durango mount.

In contrast to ^{4}He/^{3}He release spectra from the front Durango mount, the shards from the down-beam HZB3-DUR2 and HZB3-DUR3 mounts either revealed release spectra with a relative ^{3}He enrichment, with a gradual increase in ^{4}He/^{3}He from ~0.90 to ~1.00 ratios at $\Sigma F_{^3He} < 0.25$, or near-uniform ^{4}He/^{3}He release spectra (Figure 5). Nearly every shard analyzed from both HZB3-DUR2 and HZB3-DUR3 mounts yielded ^{4}He/^{3}He ratios that increased to >1.00 at $\Sigma F_{^3He} > 0.97$ (Figures S5 and S6 in Supporting Information S1).

4.3.4. HZB4 Irradiation

A fourth irradiation was conducted in January 2023 with the motivations to (a) improve the axial ^{3}He flux to improve the uniformity of ^{3}He in each mounted grain across the assembly, (b) assess the potential of computer simulations to inform optimum sample-assembly geometries, and (c) minimize the wait time following irradiations for safe handling. To minimize the total activation of the sample mounts, pure aluminum washers with a larger inner diameter were used as the replacement of stainless steel. An identical sample assembly holder to that used in the third HZB irradiation was employed except a total of five samples were included with an axial spacing of 2 mm (informed by computer simulations). Durango sample mounts were again included in the front and back

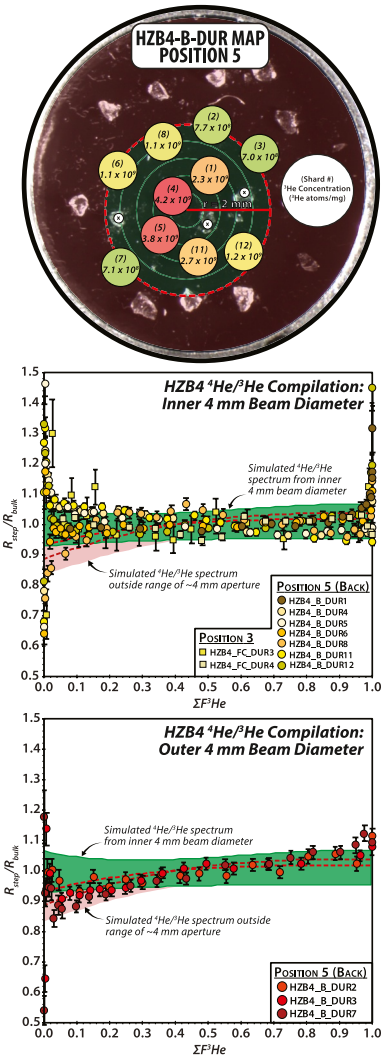

Figure 6. *Summary of the fourth Helmholtz Zentrum Berlin (HZB4) irradiation experiment with a ^{3}He concentration map of the back Durango apatite mount analyzed and a compilation of single-shard ^{4}He/^{3}He release spectra obtained from radial locations within and outside a* 2mm *radius (radius of aperture) from the proton beam center.* Durango shards within the inner 2 mm radius showed improved ^{3}He uniformity compared with the results from the third HZB3 irradiation, with selected shards revealing a moderate depletion of ^{3}He (^{4}He/^{3}He ratio of ~1.5–1.6) at $\Sigma F_{^3He} < 0.2$. Shards outside the 2 mm radius show a systematic enrichment of ^{3}He at $\Sigma F_{^3He} < 0.2$. Simulation results derived from Figures 8 and 9 are imposed in green (inner 2 mm) and red (outer 2 mm), and the simulated ^{4}He/^{3}He release spectra agree typically within ~5% with the observed release spectra.

sample positions, whereas euhedral apatite with unknown ^{4}He distributions from selected samples were mounted in positions 2–4. Each unknown sample mount included Durango shards strategically mounted near natural grains with a similar size. These shards were mounted as a quality control for the uniformity of ^{3}He induced at that specific location. Similar to the HZB3 irradiation, the samples were exposed to a primary average beam current of ~42 nA for 3,600 s. The irradiated samples were safe to handle and transport 2 weeks after the irradiation.

A total of 10 Durango shards were analyzed for ^{4}He/^{3}He release spectra from the back mount (position 5), and 2 Durango shards were analyzed from the unknown sample mount in position 3 (Figure S7 in Supporting Information S1). After mapping out the ^{3}He concentrations on the back mount, the position of the beam center was estimated. Shards within the inner 2 mm radius from the beam center yielded bulk ^{3}He concentrations ranging from 1.1 to 4.2 × 10^9 atoms/mg (average of 2.3 × 10^9 atoms.mg), whereas shards analyzed outside the 2 mm radius (outside aperture range) had markedly lower ^{3}He concentrations between 7.0 and 7.7 × 10^8 atoms.mg (average of 7.3 × 10^8 atoms/mg) (Figure 4d). Bulk ^{4}He concentrations from all shards ranged from 3.2 to 5.2 × 10^{12} atoms/mg, with an average of 4.4 × 10^{12} atoms/mg.

Out of the Durango shards from positions 3 and 5 from the inner 2 mm beam-radius, 8 out of 9 shards generally showed near-uniform ^{4}He/^{3}He release spectra within a 5% margin of 1.00 (Figure 6). One shard (HZB4-B-DUR8) near the outer 2 mm radius revealed a systematic steep increase in ^{4}He/^{3}He ratios from ~0.80 to 1.00 at $\Sigma F_{^3He}$ 0.00–0.10 that stabilized to a ratio of ~1.00 at $\Sigma F_{^3He} > 0.10$. In contrast, a shard within the inner ~1 mm beam radius (HZB4-B-DUR11) revealed a rim comparatively depleted in ^{3}He, with ^{4}He/^{3}He ratios gradually decreasing from 1.10 to 1.00 from $\Sigma F_{^3He}$ 0.00–0.25. All three shards analyzed outside the 2 mm beam-radius revealed an enriched ^{3}He rim with a systematic increase in ^{4}He/^{3}He ratios from ~0.85 to 1.00 at $\Sigma F_{^3He} < 0.30$ (Figure 6). Nearly every shard analyzed revealed sporadic ^{4}He/^{3}He ratios at $\Sigma F_{^3He} < 0.02$, whereas approximately half of the HZB4 shards revealed ^{4}He/^{3}He ratios that increased to >1.00 at $\Sigma F_{^3He} > 0.97$.

5. Discussion

5.1. Irradiation Facility and Protocol Comparison: ^{3}He Concentration and Uniformity

5.1.1. FHB Irradiated Durango: Reference for Comparison

Individual Durango shards irradiated at FHB consistently yielded near-uniform normalized ^{4}He/^{3}He ratios of 1.00 ± 0.05 throughout each degassing experiment with sufficiently high concentrations of spallation ^{3}He (Figure 2), and thus provide a reliable reference to evaluate the quality of both PSI and HZB irradiations. Regarding general ^{3}He uniformity, ^{4}He/^{3}He release spectra obtained here from individual FHB-irradiated Durango shards (^{3}He concentration ~10^9 atoms/mg) compare well with a previously published ^{4}He/^{3}He release spectrum obtained from analyzing an aggregate of multiple Durango shards (^{3}He concentration of ~10^8 atoms/mg) (Shuster et al., 2004). However, detailed analyses on select individual Durango shards revealed a systematic increase in ^{4}He/^{3}He to values >1.0 at $\Sigma F_{^3He} > 0.97$, which is in contrast to the decrease in ^{4}He/^{3}He ratios observed in the final heating steps of Shuster et al. (2004). Furthermore, probing into the $\Sigma F_{^3He} < 0.02$ within large Durango shards at high resolution (~3–4 steps) systematically revealed sporadic ^{4}He/^{3}He ratios that significantly deviated from 1.0. This complex behavior is further discussed in Section 5.1.4 following the comparison of PSI and HZB irradiations below.

5.1.2. Comparison of PSI and FHB Irradiations

Whereas PSI-irradiated Durango shards yielded comparatively uniform $^4He/^3He$ release spectra with consistent bulk ^3He concentrations, the average ^3He concentration of 7.5×10^7 atoms/mg induced within each shard is an order of magnitude lower than the concentration required to ensure that sufficient ^3He can be measured from natural apatite with typical grainsizes of ~60–150 μm (particularly during low-temperature heating steps) (Figure 3). The PSI and FHB protocol and sample assembly differed in only two major aspects: (a) PSI-Durango shards were first closely packed within Parafilm®-packs instead of Al foil-packets used in the FHB irradiation, before being placed within individual HDPE capsules and (b) the PSI proton flux was ~1–2 orders of magnitude lower than the FHB flux (Figure 1). The use of Parafilm® (a hydrocarbon polymer) is unlikely to have negatively impacted the uniformity of induced ^3He; it may be a preferred material to homogenize the composition of the target-sample assembly because the Parafilm® composition is more similar to that of the HDPE capsules, minimizing the activation of metals like Al that result in comparatively longer-lived radionuclides following proton bombardment (Bäumer et al., 2019). The consistency of uniform $^4He/^3He$ release spectra and bulk ^3He concentrations observed within individual shards from both FHB and PSI irradiations indicates that this "conventional" protocol and sample-target assembly is well-suited for the $^4He/^3He$ method, as long as the minimum ^3He concentration is met. However, due to safety regulations that limit the maximum proton beam current to 2 nA (maximum flux of $\sim 2 \times 10^9$ protons/cm^2/s) at PSI, reaching the required minimum fluence of $\sim 10^{15}$ protons/cm^2 would require ~140 hr-long irradiations—a logistical infeasibility. Although PSI irradiations may be considered suitable for stepped-heat ^3He degassing experiments on individual crystals >300 μm, this irradiation was unfortunately not sufficient to analyze the smaller individual crystals most common in natural samples.

5.1.3. Comparison of HZB and FHB Irradiations

The irradiation protocol tested at HZB significantly differed from that of FHB in terms of beam energy (69 vs. 229 MeV), primary beam diameter (3 vs. 13 mm), maximum intensity ($\sim 10^{12}$ vs. $\sim 10^{11}$ protons/cm^2/s), irradiation medium (in-vacuum vs. atmosphere), and target-sample assembly (single layer apatite tape mount vs. stack of HDPE capsules) (Figure 1). These major differences required a developmental period during which a total of four irradiations have been conducted on Durango apatite at HZB to date—each irradiation has significantly improved the quality of ^3He uniformity and our understanding of the mechanisms at play. In this section, we primarily focus on the results from our most recent HZB4 irradiation, yielding the highest quality results. The HZB4 results summarized in Figure 6 indicate that the rapid proton irradiation protocol has significant promise to induce high concentrations of ^3He uniformly within Durango apatite. Compared to the compiled $^4He/^3He$ release spectra of FHB-irradiated Durango shards (Figure 2), it is apparent that the HZB4 irradiation results lack the same level of consistency in $^4He/^3He$ release spectra. Furthermore, two of the nine total shards within the inner 2 mm beam radius revealed both anomalously enriched and depleted ^3He rims, and these inconsistencies are difficult to reconcile beyond the potential explanation that the incident proton beam was not perfectly radially symmetrical. Despite these inconsistencies, the majority of HZB4-irradiated Durango shards revealed uniform $^4He/^3He$ release spectra, and the HZB protocol allows a direct quality assessment of both ^3He concentration and uniformity expected at any one location by mounting Durango shards at multiple locations within the sample stack. Furthermore, observed $^4He/^3He$ release spectra from both HZB3 and HZB4 irradiations agree well with their respective simulations (see Section 5.2.2), which allows the use of PHITS simulations to optimize irradiation parameters to improve the consistency in future HZB irradiations.

5.1.4. Systematic Observations in All Irradiations

When the initial and final ~10% of the $\Sigma F_{^3He}$ from analyzed Durango shards were probed at sufficiently high resolution for $^4He/^3He$ ratios, two distinct trends were observed regardless of the irradiation protocol: (a) $^4He/^3He$ ratios at $\Sigma F_{^3He} < 0.02$ were highly variable, and often revealed a trend of ^3He enrichment in the first step, followed by ^3He depletion before stabilizing to consistent ratios at $\Sigma F_{^3He} > 0.02$ and (b) a near-exponential increase in $^4He/^3He$ ratios at $\Sigma F_{^3He} > 0.97$ (Figures 2, 3, 5, and 6). Although inconsistent $^4He/^3He$ ratios from previous studies have been attributed to low ^4He concentrations during initial extraction steps with notably higher and variable ^4He blanks (Shuster & Farley, 2005), we note that the ^4He and ^3He signals from our initial stepped-heating measurements were sufficiently above blank levels. Furthermore, whereas spallation ^4He is produced during proton irradiation at rates ~8–10 times higher than ^3He, the abundance of spallation ^4He is orders of

magnitude lower than radiogenic ^{4}He within the Durango shards such that spallation ^{4}He can be assumed to have a negligible effect on the observed ^{4}He/^{3}He release spectra.

We consider that the spurious ratios at $\Sigma F_{3He} < 0.02$ reflect an irradiation-induced edge effect, which may reflect micron-scale spatial inhomogeneities in the ^{3}He distribution caused by surface sputtering and/or recoil loss of ^{3}He at the rim (MacDonald, 1970). Recoil loss of ^{39}Ar during neutron irradiation has been extensively studied due to its impact on ^{40}Ar/^{39}Ar age profiles, and shows a significant grain-size dependence (e.g., Foland et al., 1992; Hall, 2013; Huneke & Smith, 1976; Jourdan et al., 2007). However, there is no apparent relationship between grain size and the observation of spurious ratios at $\Sigma F_{3He} < 0.02$—this effect was also apparent in selecting HZB4 Durango shards that yielded broader-scale irradiation induced rim enrichment of ^{3}He (HZB4_Back_DUR3 and 7). We thus consider that this edge effect is most likely linked to the impact of sputtering at the grain surface, but further work is required to evaluate and potentially amend this effect. Despite its potential to impact on the first stepped heating measurements on natural samples, the average ratios of each point $\Sigma F_{3He} < 0.02$ generally balance out to adhere to the broader ^{4}He/^{3}He release spectrum. Thus, this sporadic behavior likely will not be observed if the first heating step extracts ∼2%–3% of the bulk gas.

The observed systematic increase in ^{4}He/^{3}He ratios at $\Sigma F_{3He} > 0.97$ was striking in that this observation contrasts the downward trend in ratios in the final heating steps reported by Shuster et al. (2004). The only major experimental difference between these contrasting observations is that we report ^{4}He/^{3}He release spectra from individual shards (∼300–400 μm) as opposed to an aliquot with multiple shards (∼75–220 μm). The mechanism behind these opposing observations remains uncertain, but we speculate that our observed increase in ^{4}He/^{3}He ratios may be the result of a mass-dependent effect on helium diffusivity—the increasing trend closely matches the modeled ^{4}He/^{3}He release spectra of Shuster et al. (2004) based on the inverse root mass relationship ($D^{4He}/D^{3He} = (m_3/m_4)^{(1/2)} = 0.868$). Unfortunately, the temperature accuracy from our diode-laser heating was not yet suitable at the time of experiments to assess potential differences in ^{3}He and ^{4}He diffusivities with confidence.

Alternatively, the observed increase in ^{4}He/^{3}He may be irradiation-induced, with shards from our experiments exhibiting a core depleted in ^{3}He. A depleted ^{3}He core may result from the preferential implantation of ^{3}He from surrounding sources along the crystal's rim. If this is true, this effect on ^{4}He/^{3}He release spectra may be dependent on both the stopping range of implanted ^{3}He and grain-size. Whereas we irradiated larger individual Durango shards than Shuster et al. (2004) (∼300–400 μm compared to ∼75–220 μm shards), it could be possible that if the stopping range of implanted ^{3}He exceeds the radius of smaller crystals, the irradiated shards of Shuster et al. (2004) may have a relatively enriched ^{3}He core (resulting in the observed downward ^{4}He/^{3}He trend). In contrast, if the average stopping distance of implanted ^{3}He is less than the grain radius, there may be a relative depletion of ^{3}He in the core. We note, however, that if these observed differences were dependent on grainsize, the ΣF_{3He} at which the ^{4}He/^{3}He shift initiates would likely vary and not be exclusive to the consistently observed shift at $\Sigma F_{3He} > 0.97$. Resolving the mechanism for the observed difference in ^{4}He/^{3}He ratios from $\Sigma F_{3He} > 0.97$ remains beyond the scope of this study, but we note that this observation has significant potential implications for (a) the use of ^{3}He as a direct proxy for natural radiogenic ^{4}He diffusivities, and (b) the assessment of how potential high-temperature helium traps may impact ^{4}He/^{3}He ratios (e.g., Guo et al., 2021).

5.2. Assessment of Axial and Radial ^{3}He Flux From HZB Irradiations

5.2.1. Observations

Following the radial mapping of ^{3}He concentrations on HZB2 Durango shards mounted in the front position (in first contact with proton beam) and the back position, it became apparent that the ^{3}He flux was both radially and axially (in beam direction) variable. This was particularly apparent in the HZB2 irradiation results before beam scattering was implemented because the radial ^{3}He concentration distribution in the front mount revealed a rapid decline in induced ^{3}He concentrations within a distance of only ∼0.5 mm, whereas the radial ^{3}He concentration was both greater and more uniform in the back sample (Figure 4). The distinct strong gradient in the radial ^{3}He concentration distribution from the front mount (also observed in the HZB1 irradiation) directly reflects the Gaussian distribution of the primary beam intensity, which was notably narrower than initially anticipated.

Following the implementation of a tantalum scattering foil placed up-beam from the samples to broaden the proton beam in HZB3 experiments, we further assessed the radial and axial ^{3}He distribution with ^{4}He/^{3}He release spectra. Maps of bulk ^{3}He concentrations from the HZB3 irradiation revealed a notable improvement in the radial

uniformity induced within Durango shards mounted in the front, indicating the effectiveness of the scattering foil (Figure 4e). The radial ^{3}He distribution induced in shards from two separate down-beam mounts resembled that from the front mount, but individual shards from each down-beam mount typically yielded higher concentrations than those from the front mount.

^{4}He/^{3}He release spectra from nearly all front-mounted HZB3 Durango shards revealed a systematic depletion in ^{3}He at $\Sigma F_{3He} < 0.40$, whereas ^{4}He/^{3}He release spectra from the majority of down-beam shards reveal the presence of an enriched ^{3}He rim (Figure 5). From these observations, we speculated that Durango shards in the first contact with the proton beam (front mount) will show the depletion of ^{3}He in the front rim due to the preferential down-beam migration and emplacement of spallation ^{3}He. When the proton beam contacts the front mount, spallation ^{3}He generated from the front sample mount and each subsequent mount will get transported down-beam, and lower-energy ^{3}He particles will preferentially become implanted within the front rim of mounted grains, resulting in an enriched ^{3}He rim observed in most down-beam Durango shards. We note that select down-beam Durango shards from HZB3 yielded uniform ^{4}He/^{3}He release spectra, potentially indicative of an ideal balance between the axial implantation and depletion of ^{3}He that may be geometrically controlled.

5.2.2. Simulations

5.2.2.1. Visualizing the ^{3}He Flux and Distribution

To evaluate the observed axial and radial variability in ^{3}He distribution across the HZB3 target assembly, we ran simulations using PHITS that implemented near replicate target assembly geometries, material compositions, and beam parameters (Figure 7). We simulated the axial and radial ^{3}He distribution of each sample mount position within seven 400 μm-wide concentrically increasing rings of synthetic apatite with a 300 μm thickness. The computed axial ^{3}He yield for each ring was normalized by its volume for direct comparison. For a general comparison of the axial variability from each sample mount, the computed ^{3}He distributions within the inner 2 mm radius were averaged for each sample mount for simplicity (Figure 8). To compare the general radial variability in the ^{3}He distribution, the computed distributions from each concentric ring and each sample position were averaged (Figure 9). To visualize the detailed variability in the simulated ^{3}He distribution at individual locations (i.e., non-averaged), see the supplementary material (Figures S8 and S9 in Supporting Information S1).

The HZB3 ^{3}He distribution simulations indicate that apatite mounted in the front position will receive a ^{3}He yield that increases non-linearly from the front rim to the back rim (Figure 8). This comparative depletion of ^{3}He in the front rim is most likely the result of preferential spallation-induced ejection of ^{3}He in the beam direction as a primary mechanism, and the loss of secondary ^{3}He particles from the grain surface by sputtering as a secondary mechanism (MacDonald, 1970). Simulation results reveal that when the incident proton beam contacts the first sample mount, activation of the apatite and carbon tape generates an abundance of ^{3}He that scatters and diffuses in the beam direction under vacuum conditions (Figure 7). This diffusive cloud of ^{3}He is transported down-beam to the subsequent mount, and the simulated axial ^{3}He flux within the apatite layers at multiple radial positions systemically shows relative enrichment of ^{3}He in the front rim—likely indicative of the preferential rim implantation of ^{3}He generated from the mount up-beam (Figure 8). However, near-uniform axial ^{3}He fluxes were also simulated within the apatite layer at distinct radial and mount locations. This simulated ^{3}He uniformity in the apatite layer indicates that a balance in the implantation and ejection (same mechanism for depletion observed in front mount) of ^{3}He is achieved at specific locations, which is most likely dependent on the radial intensity distribution of the scattering ^{3}He cloud when it contacts the apatite layer.

5.2.2.2. Simulated ^{4}He/^{3}He Release Spectra

By assuming that the apatite from the above simulations had a pre-irradiation uniform ^{4}He component (i.e., a Durango shard), the computed axial and radial distributions were utilized to simulate ^{4}He/^{3}He release spectrum predictions at various locations along the sample assembly (a ±5% error envelope was applied to simulated release spectra) (Figures 8 and 9). The resulting HZB3-simulated ^{4}He/^{3}He release spectra successfully predicted the majority of the measured ^{4}He/^{3}He release spectra observed from the HZB3-irradiated Durango shards (Figure 5). In particular, analyzed HZB3 Durango shards yielding both depleted ^{3}He rims (from front mount) and enriched ^{3}He rims (from down-beam mounts) were predicted remarkably well with similar magnitudes of relative depletion/enrichment (Figure 8). This agreement between observed and simulated ^{4}He/^{3}He release spectra is particularly important, as it allows utilizing these simulations in attempts to improve the quality of future

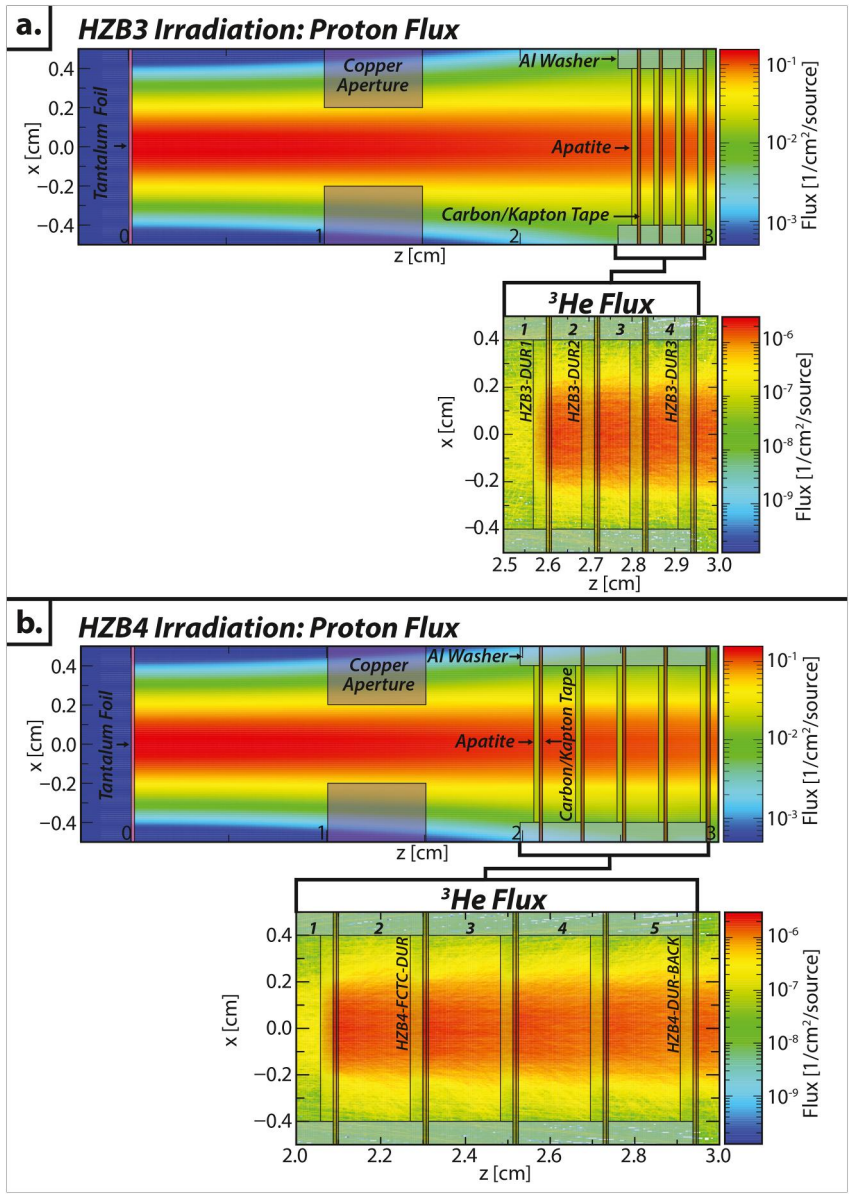

Figure 7. *Simulated proton and ^{3}He fluxes across the sample assembly for the third* (a, *HZB3*) *and fourth* (b, *HZB4*) *irradiations at the Helmholtz Zentrum Berlin*. Once the proton beam interacts with the first sample mount in position 1, spallation ^{3}He is generated, transported down-beam, and each subsequent sample is exposed to this scattering cloud of externally produced ^{3}He. The only parameter changed between the HZB3 and HZB4 irradiation was the spacing of each sample mount from 1 to 2 mm, which was intended to reduce the intensity of the ^{3}He flux exposed to each apatite layer to reduce induced an enriched ^{3}He front rim observed in the HZB3 irradiation.

irradiations—various material compositions and geometries can be adjusted to optimize the uniformity of the axial and radial ^{3}He flux across the sample assembly target.

5.2.3. Informing HZB Irradiations With Simulations

We ran a series of PHITS simulations prior to the HZB4 irradiation in an attempt to define a single parameter that could be adjusted to improve the quality of the irradiation. One observation from previous simulations is that the intensity of the generated ^{3}He cloud behind each mount dissipates down-beam due to scattering; therefore, we hypothesized that increasing the spacing between sample mounts may expose the apatite layer to a more uniform

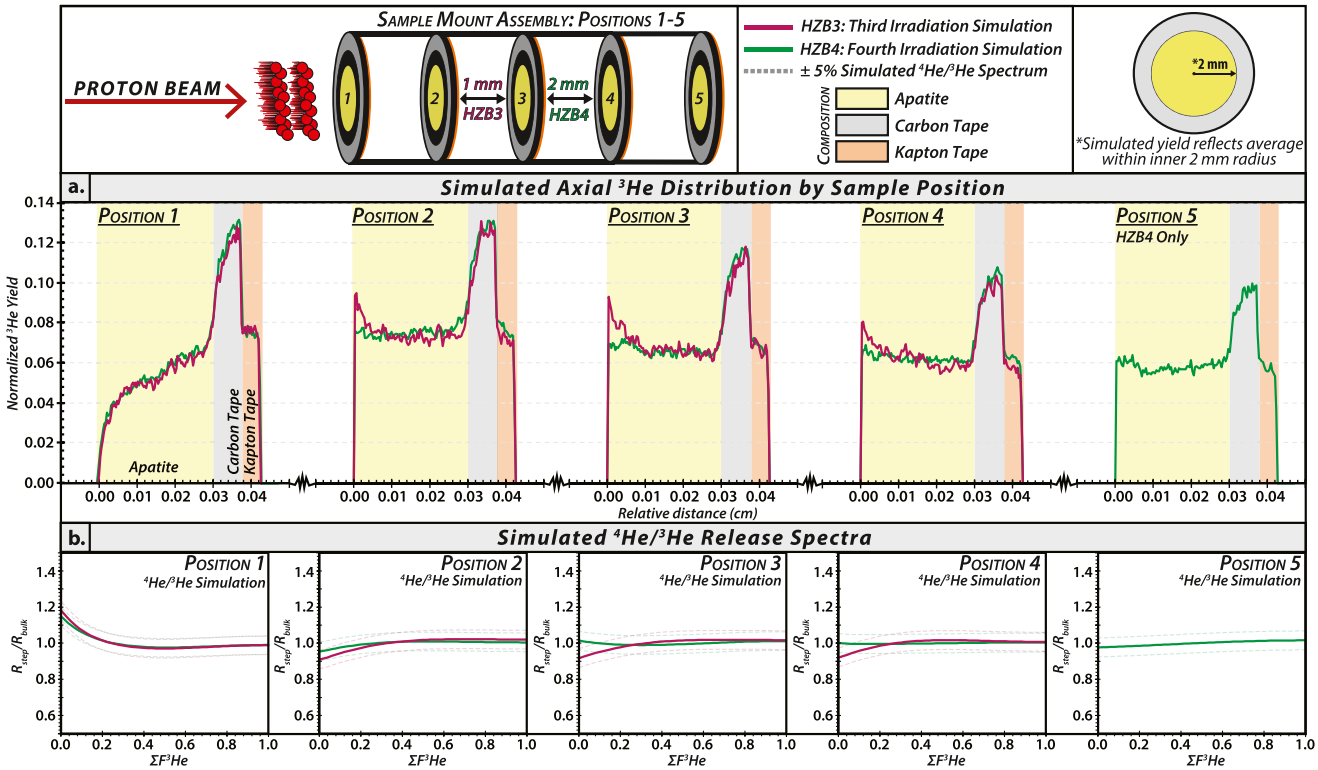

Figure 8. *Simulated axial ^{3}He distributions for each sample mount position and their corresponding ^{4}He/^{3}He for the third and fourth Helmholtz Zentrum Berlin irradiation experiments* (*HZB3 and HZB4*, *respectively*). (a) The apatite layer in the front mount will always induce a front rim depleted in ^{3}He. When the sample spacing was set a 1 mm (e.g., HZB3), a spike in the ^{3}He yield within the front rim of each down-beam sample mount was simulated, likely due to preferential implantation during exposure to an intense ^{3}He flux generated up-beam. In contrast, the simulation suggests that this implantation effect can balanced out by implementing a sample mount spacing of 2 mm (HZB4), which will improve the uniformity in the axially induced ^{3}He distribution. (b) Simulated axial and radial distributions were utilized to simulate predicted ^{4}He/^{3}He release spectra for each position under the assumption that each simulated apatite layer contained a uniform ^{4}He distribution. Simulated HZB3 ^{4}He/^{3}He release spectra predict relatively enrichment of ^{3}He at $\Sigma F_{^{3}He} < 0.2$, whereas simulated HZB4 release spectra predict near-uniform ^{4}He/^{3}He release spectra.

and less intense flux of ^{3}He that will be implanted at the front of the down-beam mount. Simulations reveal that, after adjusting the axial spacing of the sample mount from 1 mm (implemented in the HZB3 irradiation) to 2 mm (Figure 7), it is possible to significantly reduce the ^{3}He rim enrichment effect observed in the HZB3 irradiation (Figures 8 and 9). Simulations also indicate that ^{3}He uniformity may be improved by implementing different mounting materials. For example, we show that the carbon tape generates comparatively more ^{3}He than the apatite layer (based on compositional differences in activation), and thus the intensity of the ^{3}He cloud may be lessened by implementing a different material for grain mounting such as Kapton tape. However, we preferred to only alter a single parameter for the HZB4 irradiation for a consistent assessment, and we chose to increase the sample spacing for the HZB4 irradiation to 2 mm—adjusting the materials may be implemented in future studies.

Upon obtaining ^{4}He/^{3}He measurements on HZB4-irradiated Durango shards, nearly all observed ^{4}He/^{3}He release spectra agree within the error of the simulated ^{4}He/^{3}He release spectrum predictions (Figure 6). Furthermore, even the ^{3}He enriched front rim in HZB4 Durango shards outside the 2 mm radius with notably lower bulk ^{3}He yields were predicted by the simulations and confirmed by the measurements. This behavior was likely the result of the copper aperture absorbing much of the proton beam energy and intensity, which would limit the total in situ production of ^{3}He outside the 2 mm radius. Durango shards outside the 2 mm beam-radius will likely have an enrichment of ^{3}He in the front-facing rim sourced from ^{3}He that is produced within the inner 2 mm up-beam mount, but scatters beyond the 2 mm radius in the down-beam mount and implanted within the apatite in a radial region where the aperture has absorbed much of the beam energy and intensity—this scattering influence can be visualized in Figure 7. The overall improvement in ^{3}He uniformity from the HZB3 to HZB4 irradiations, and the notable consistency in simulated and observed ^{4}He/^{3}He data from both irradiations indicate that PHITS simulations provide a powerful means to assess and inform current and future irradiations.

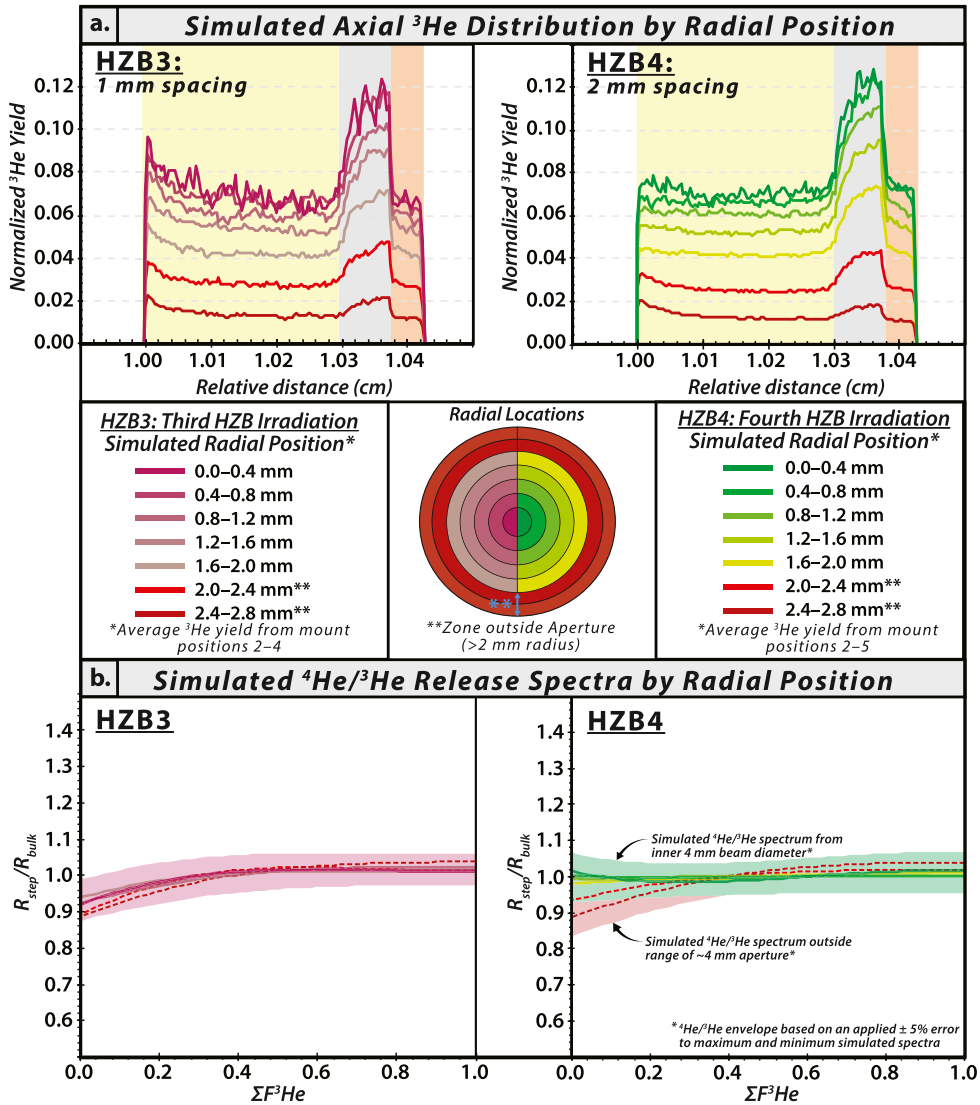

Figure 9. *Simulated radial ^{3}He distributions averaged from each sample mount position (excluding position 1) with their corresponding ^{4}He/^{3}He release spectra for the third and fourth Helmholtz Zentrum Berlin irradiation experiments (HZB3 and HZB4, respectively).* (a) Normalized ^{3}He distributions simulated at varying radial positions (binned by 0.4 mm rings) indicate that within the inner 2 mm beam-radius, the general axial pattern in the ^{3}He remains systematic with a gradual decrease in ^{3}He yield away from the center. Outside the 2 mm radius (i.e., outside of aperture range), the ^{3}He yield decreases substantially, and an enriched front rim is simulated for HZB4 irradiation. (b) Predicted ^{4}He/^{3}He release spectra from the simulated distributions suggest minimal radial variability should be expected within the inner 2 mm beam-radius for each respective irradiation experiment. However, simulated release spectra outside the 2 mm beam-radius for the HZB4 simulation predict an enrichment of ^{3}He at $\Sigma F_{^{3}He} < 0.2$, which was observed in HZB4 irradiated Durango shards (Figure 6).

5.3. Apparent Versus True ^{3}He Uniformity

In assessing the uniformity of ^{3}He induced within Durango apatite shards following proton bombardment, it is worth discussing the idea that a flat ^{4}He/^{3}He release spectrum with a constant 1.00 ratio may not always reflect true ^{3}He uniformity. As shown in Figure 10, if the axial and radial ^{3}He flux varies linearly from one rim to the other (at any order of magnitude difference), the averaged rim-to-core ^{3}He distribution will balance to a horizontal slope, which will result in a uniform ^{4}He/^{3}He release spectrum for a Durango shard that could be misinterpreted as ^{3}He uniformity. However, a non-uniform ^{4}He/^{3}He release spectrum will result if the induced axial and/or radial ^{3}He distribution is non-linear or non-symmetrical. This is important to illustrate because gradients exist in the incident proton beam that will directly influence the ^{3}He flux. The radial distribution of the proton-beam intensity

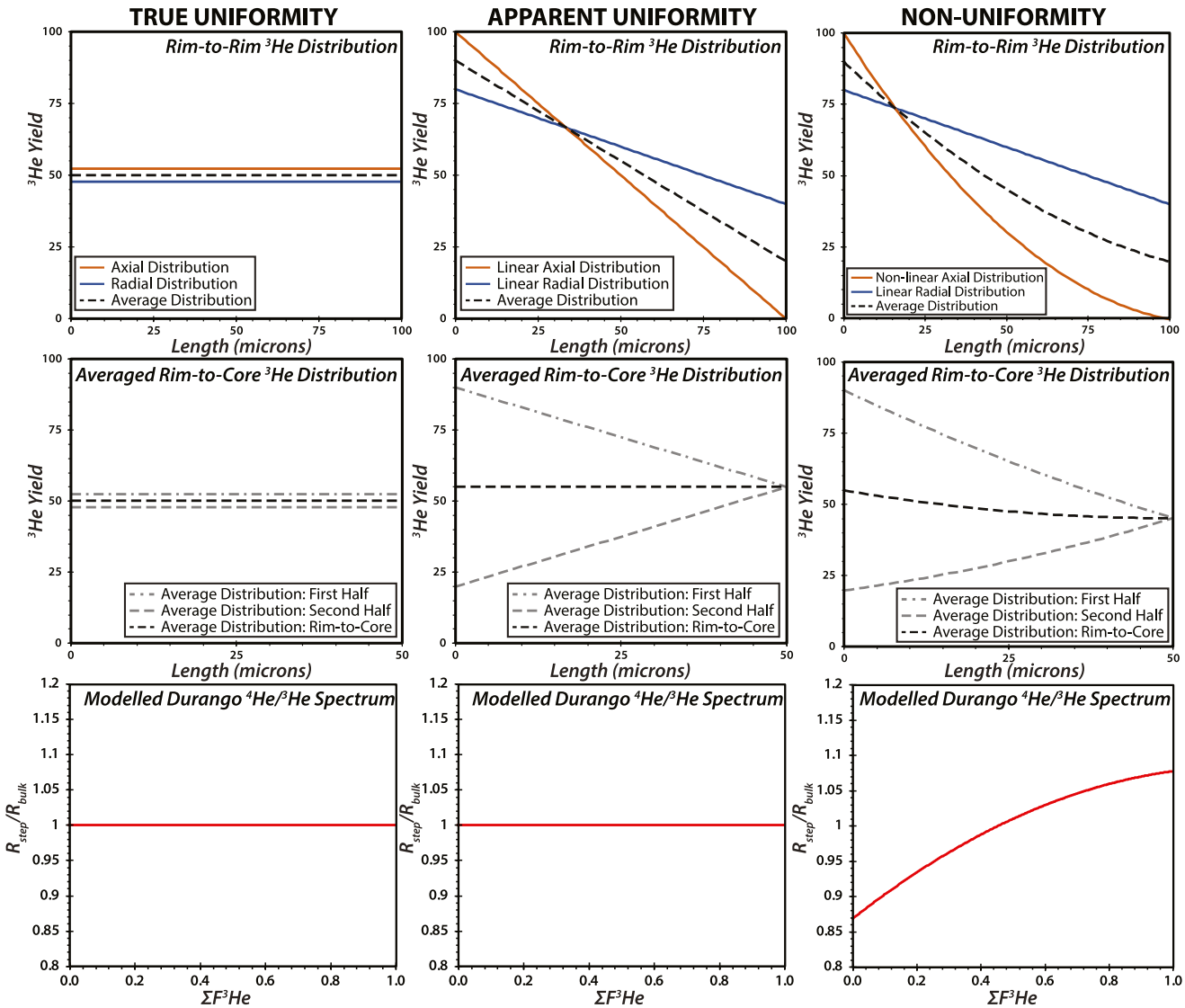

Figure 10. *Schematic demonstration of how ^{3}He distribution variability in a Durango shard may result in uniform, apparently uniform, and non-uniform ^{4}He/^{3}He release spectra*. If the axial and radial distribution induced within a Durango shard is linear or symmetrically increasing or decreasing (even on extreme gradients), a flat ^{4}He/^{3}He release spectrum with a constant 1.00 ratio will be measured.

is Gaussian in shape, whereas the beam energy and intensity gradually dissipate axially. Although proton-beam gradients may not be linear at the broad scale (>0.5 mm), these gradients are effectively linear or even non-variable, at the scale of most natural apatites (~60–150 μm). Thus, if the ^{3}He distribution implanted within the sample were to directly reflect potential linear gradients in the proton beam, a Durango sample could yield an apparently uniform ^{4}He/^{3}He release spectrum. However, preferential ^{3}He implantation, depletion, or sputtering in the axial direction—as well as potential exposure to a non-linear proton beam gradient—within a Durango sample will induce a non-linear ^{3}He distribution that will result in non-uniform ^{4}He/^{3}He release spectra.

It is clear from the HZB3-irradiated Durango shards that the non-linear axial ^{3}He distribution was the primary contributor to the observed non-uniform ^{4}He/^{3}He release spectra. However, Durango shards analyzed off-center of the beam may have received a linearly variable ^{3}He yield to varying degrees. After scattering the primary Gaussian shaped 3 mm proton beam at HZB, the simulated radial ^{3}He flux across a 3 mm diameter at the end of the sample assembly varies by ~25%. However, the ^{3}He flux effectively varies linearly by ~2%–4% within the inner 1 mm beam diameter, and by ~10% within the inner 2 mm diameter. At the 100 μm scale, the radial flux varies by <2% within the inner 1.0 mm beam radius, whereas the 100 μm flux can vary by ~4%–5% within the

outermost 1.5 mm beam radius. The aim for irradiations at HZB is to minimize this radial variance by mounting and analyzing grains only within the inner 1 mm radius; however, it remains uncertain how a moderate linear radial flux may impact general $^4He/^3He$ analyses if the effect is balanced in the rim-to-core flux. The implication of a linearly variable ^3He flux may also hold true for samples routinely analyzed at FHB—recent in situ $^4He/^3He$ microprobe analysis on shards of Sri Lanka zircon irradiated at FHB revealed a spatial gradient in acquired $^4He/^3He$ ratios most likely attributed to proton beam gradients at the ∼500 μm scale (Vermeesch et al., 2023). Although we observed near uniform $^4He/^3He$ release spectra in FHB, PSI, and HZB4-irradiated Durango shards, we note the possibility that the ^3He concentration synthesized in these shards may only be apparently uniform. While confirming apparent versus true ^3He uniformity is beyond the scope of this study, establishing if such gradients—as long as they are symmetrical from rim-to-rim—impact routine $^4He/^3He$ analyses on minerals with unknown, non-uniform ^4He distributions remains an important concern worthy of detailed assessment.

5.4. Potential $^4He/^3He$ Irradiation Correction

It is clear from our results that axial and radial variability, as well as other unknown factors, in the ^3He flux from HZB irradiations may induce ^3He non-uniformly in the irradiated target material. However, we show that in applying our most recent HZB4 irradiation protocol, ^3He uniformity is consistently achieved when the irradiated materials are within a ∼1–2 mm radius of the proton beam center. When ^3He uniformity was not achieved in both HZB3 and HZB4 irradiations, we found that the non-uniform $^4He/^3He$ release spectra were systematic in both scenarios when ^3He is preferentially implanted or depleted in the front rim. In view of the observed consistency in both observed and simulated data, we propose the potential to apply a $^4He/^3He$ irradiation correction to natural samples in situations where it is likely that a non-uniform ^3He distribution was synthesized. In the irradiation of natural samples for $^4He/^3He$ applications at HZB, individual grains will be preferentially mounted within the inner 0.5 mm radius of the mount, and Durango shards of similar grain size will be systematically mounted near the natural samples. The addition of Durango standards placed at multiple location across the target assembly will serve as a quality control—similar to the use of fluency monitors for neutron irradiations for $^{40}Ar/^{39}Ar$ dating (e.g., Carter et al., 2023; Rutte et al., 2015)—for the irradiation in terms of monitoring the ^3He concentration and uniformity achieved in the shard's specific position. Ideally, Durango shards within the inner 2 mm beam diameter of the mount will provide a uniform $^4He/^3He$ release spectrum. However, if a Durango shard on a sample mount revealed a non-uniform $^4He/^3He$ release spectrum, we speculate that this $^4He/^3He$ release spectrum can be utilized to correct a $^4He/^3He$ release spectrum obtained from a natural crystal mounted in close proximity. This correction would use a similar approach applied for the laser-ablation down-hole elemental fractionation correction of Paton et al. (2010), but would instead involve fitting a curve to the observed Durango $^4He/^3He$ release spectrum, correcting for any deviations away from $^4He/^3He$ ratios of 1.00, and applying this same correction to the nearest natural sample under the assumption that this crystal obtained the same spatial ^3He yield. We note that this correction may only be required for the HZB irradiations if samples were not exposed to the center of the proton beam due to beam-alignment issues. A proper evaluation of the validity of this correction on natural samples is, of course, necessary before it can be routinely applied.

5.5. Advantage of HZB Irradiations

The progression toward uniformly inducing high concentrations of spallation ^3He in Durango apatite over the course of four irradiation experiments conducted at HZB indicates that this protocol may serve as a viable option for routine $^4He/^3He$ analyses. Perhaps the greatest advantages of the HZB irradiation protocol are its overall efficiency and potential to improve the throughput of $^4He/^3He$ analyses. Through established collaboration, it is feasible to schedule multiple (∼3–6+) irradiations over the course of a year, with the possibility of irradiating ∼12–15+ samples in a given day. The comparatively high-proton flux achieved in these irradiations permits reaching a minimum fluence of $\sim 10^{15}$ protons/cm^2 in less than 1 hr for each individual sample stack (including 4–5 samples), and multiple stacks may be irradiated in a single day—the viability of irradiating even more samples with thicker sample stacks will be assessed in future irradiations. Furthermore, the efficiency of this procedure is enhanced by the ability to safely transport and handle the irradiated material within only 1–2 weeks following the irradiation. This short cool-down time is made possible by minimizing the amount and variety of materials used for the irradiation, thus limiting the total activity levels of the target assembly. For example, after the HZB4 irradiation, the cumulative activity level of the irradiated material 14 days after the irradiation was 2.7×10^4 Bq—well below permissible thresholds restricting non-permitted transport and handling. Thus, with sufficient

planning, 12–15 samples collected from the field can be processed for mineral separation, irradiated, and packed for ^{4}He/^{3}He measurements in as little as two months. Indeed, it is possible to irradiate apatite grains from more than 100 samples at once with the higher energy FHB protocol; however, these irradiations (a) occur less frequently, (b) require prolonged (multiple months) cool-down periods before samples can safely be shipped, and (c) require a large sample suite of mineral separates prepared at the time of irradiation. These points are particularly important because the current timeline to obtain irradiated material—from the field-to-irradiation-to-analysis—may be out of sync with typical timelines for post-doctoral researchers, or even PhD students, who wish to apply ^{4}He/^{3}He for their studies.

5.6. Future Outlook

The reliance on methodologies such as ^{4}He/^{3}He will continue to grow as the field of low-temperature thermochronology evolves. Conventional bulk (U-Th)/He dating approaches commonly lack important grain-specific information and require several assumptions in order to address many important Earth-science issues (e.g., Colleps et al., 2022; McDannell et al., 2018). ^{4}He/^{3}He analyses not only provide information on the thermal-history dependent ^{4}He distribution within a crystal, but step-heated measurements on uniform spallation ^{3}He can be used to quantify or estimate natural ^{4}He diffusivities. With sufficient temperature control and precision on individual extraction steps, this approach potentially permits utilizing single crystals as their own unique thermochronometer, which has significant implications for studies applying (U-Th)/He thermochronology on grains with variable eU concentrations in settings ranging from ancient cratonic settings (e.g., Colleps et al., 2021; Flowers et al., 2020; McDannell et al., 2022) to modern glaciated landscapes (e.g., Valla et al., 2012). Furthermore, proton irradiation of geological material has implications beyond ^{4}He/^{3}He thermochronology; for example, proton-irradiated quartz has been utilized to calibrate and advance the growing field of cosmogenic noble gas paleothermometry (Shuster & Farley, 2005; Tremblay et al., 2014), and diffusion experiments on olivine using spallation helium and neon have been used to track noble gas inventories within the mantle over geologic time (e.g., Dygert et al., 2018). Accordingly, it remains equally important to advance the procedures required to induce uniform and high concentrations of ^{3}He in geological materials to meet the anticipated future demand for the types of desired analyses in the community.

Our FHB and PSI irradiated Durango shards reveal that the synthesis of uniform ^{3}He is most consistently achieved using the conventional sample target assembly with a broad and high-energy proton beam. We consider this conventional approach most favorable in terms of consistency; however, our progressive improvement with each irradiation conducted at HZB indicates that a similar level of consistency can be achieved after further refinement. Accordingly, future irradiations at HZB will include minor subsequent modifications to the sample assembly materials and geometries with monitoring of Durango apatite until consistency is optimized.

A potential alternative to proton irradiations for the uniform synthesis of ^{3}He is the direct implantation of ^{3}He via a ^{3}He ion beam with modulated energy variability. The stopping distances of ^{3}He in apatite from 1 to 185 μm correspond to beam energies ranging from ∼0.3 to 20.0 MeV (Ziegler et al., 2010). The consistent modulated exposure of apatite crystals across this range of energies—assuming that the flux remains constant at each energy level—could theoretically implant ^{3}He uniformly in individual crystals at exceptionally high concentrations. Direct implantation of ^{3}He has previously been utilized to characterize helium diffusion in both zircon and apatite (Cherniak, 2019; Cherniak et al., 2009); however, these implantation experiments were specifically adapted for Nuclear Reaction Analyses and used a mono-energy ^{3}He beam of 100 keV to implant ^{3}He to a specific depth within ∼0.5 mm-thick polished mineral slabs. Direct ^{3}He implantation is advantageous in that (a) the required energies are sufficiently low to avoid major activations and production of secondary ions within the samples and (b) the distribution of ^{3}He can directly be controlled without the need to balance ^{3}He ejection and implantation. A potential issue is that the amount of lattice damage induced by a ^{3}He beam per source is greater than that induced by a proton beam. However, in reference to the average ^{3}He concentration of $\sim 3.2 \times 10^9$ atoms/mg generated within Durango apatite from the FHB irradiation, a lower total ^{3}He implantation fluence of $\sim 3.2 \times 10^{12}$ ^{3}He/cm^2 would be required to equal the concentrations of ^{3}He induced via proton irradiation, with a total fluence of $\sim 1 \times 10^{16}$ protons/cm^2. Thus, when considering (a) the significant difference in the required fluences between ^{3}He implantation and proton irradiation and (b) the total damage from secondary products produced in proton irradiation (including damage from spallation ^{3}He), the cumulative damage from implantation would be comparable to that induced during proton irradiations. We ran simulations in PHITS to illustrate the difference in DPA (e.g., Iwamoto et al., 2012) for high-energy proton (100 and 250 MeV) and low energy ^{3}He (∼1 MeV) beams

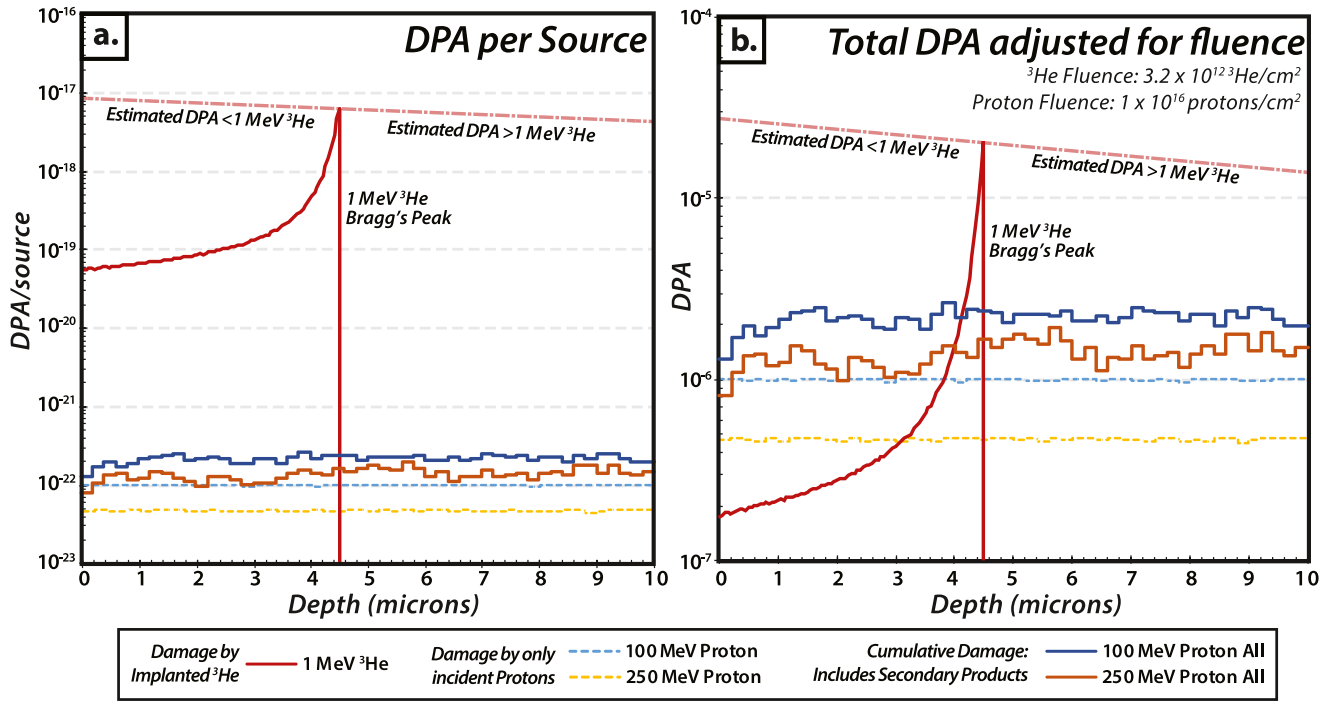

Figure 11. *Simulations of the relative damage (in displacements per atom [DPA]) induced by high-energy proton beams and a primary ^{3}He beam for direct implantation.* Although the total DPA per ion is notably greater for a ^{3}He particle (a), adjusting this for the total required proton and ^{3}He fluence required to induce sufficient ^{3}He within apatite suggests that the total difference in damage between the two methods is relatively similar (b).

induced at a 100 μm-scale within an infinite apatite cylinder. As shown in Figure 11, the total DPA/source from the primary ^{3}He at the location of implantation is far greater than that from a proton beam (including damage from secondary products); however, when the required fluences of the ^{3}He and proton beam exposure are normalized to those required to achieve $\sim 3.2 \times 10^{12}$ ^{3}He/cm^2, the total DPA from proton irradiations (normalized to a fluence of 1×10^{16} protons/cm^2) is comparable to that induced by implantation. We note that ^{3}He was implanted on the order of $\sim 10^{15}$ ^{3}He/cm^2 in the experiments of Cherniak et al. (2009) under the argument that implantation-induced lattice damage was negligible. Accordingly, as it is likely that lattice damage from bulk-grain ^{3}He implantation has negligible effect on helium diffusivities, this approach may serve as a promising future alternative to proton-irradiations for ^{4}He/^{3}He and diffusion-based studies.

6. Conclusions

The compilation of ^{4}He/^{3}He release spectra and bulk ^{3}He concentrations measured from internal shards of Durango apatite irradiated at three separate facilities indicate that the proton-irradiation procedures previously established at the FHB are most consistent in inducing uniform and high concentrations of ^{3}He within geological materials. A similar-type protocol was employed at PSI, and although these irradiations induced uniform ^{3}He within Durango shards, a restriction on the maximum permitted proton flux prevented the samples from reaching the required ^{3}He concentration for typical ^{4}He/^{3}He analyses on small individual crystals within a reasonable irradiation duration. An alternative high-intensity and rapid proton irradiation protocol was developed at HZB involving in-vacuum irradiations with a comparatively narrow beam. Over the course of four HZB irradiations, the protocol has evolved with the assistance of PHITS computer simulations to show great potential at inducing high and uniform concentrations of ^{3}He with significantly improved efficiency. Whereas ~20% of the measured Durango shards from the fourth HZB irradiation (HZB4) revealed inconsistent ^{4}He/^{3}He release spectra with enriched or depleted ^{3}He rims, this protocol will only evolve over time to further improve the consistency of ^{3}He uniformity across the sample target in future irradiations. Major benefits of this protocol include (a) samples can reach the required proton fluence within 1 hr irradiations; (b) the quality of the irradiation can be directly monitored by mounting shards of Durango apatite at various axial and radial positions across the target; (c) multiple irradiations may be conducted in rapid succession; and (d) this protocol minimizes the amount of

material activated, which allows the irradiated samples to be safely handled within 1–2 weeks after the irradiation. Accordingly, the incorporation of the HZB-irradiation protocol has great potential to improve both the accessibility and throughput of $^{4}He/^{3}He$ analyses.

Data Availability Statement

All data generated in this study are readily available in Supporting Information S1 and supporting data files are archived at Colleps et al. (2024) (https://doi.org/10.5281/zenodo.10532069).

Acknowledgments
This work was supported by the European Research Council (ERC) under the European Union's Horizon 2020 research and innovation programme (ERC Advanced Grant 834271 to P.v.d.B). The authors thank Dr. Wojciech Hajdas for his support for the irradiation conducted at the Paul Scherrer Institute. The authors also thank David Shuster and Florian Hofman for their meticulous reviews that helped improve the quality of this paper. Open Access funding enabled and organized by Projekt DEAL.

References

Amalberti, J., van der Beek, P., Colleps, C., Bernard, M., & Wapenhans, I. (2023). *New high-resolution step heating experiments using a coupled Diode laser and thermocouple for thermochronology applications*. Copernicus Meetings. https://doi.org/10.5194/egusphere-egu23-6766

Bäumer, C., Bäcker, C. M., Gerhardt, M., Grusell, E., Koska, B., Kröninger, K., et al. (2019). Measurement of absolute activation cross sections from carbon and aluminum for proton therapy. *Nuclear Instruments and Methods in Physics Research Section B: Beam Interactions with Materials and Atoms*, *440*, 75–81. https://doi.org/10.1016/j.nimb.2018.11.020

Brennan, C. J., Stockli, D. F., & Patterson, D. B. (2020). Zircon $^{4}He/^{3}He$ fractional loss step-heating and characterization of parent nuclide distribution. *Chemical Geology*, *549*, 119692. https://doi.org/10.1016/j.chemgeo.2020.119692

Carter, J. N., Renne, P. R., & Morgan, L. E. (2023). Potassium-39-derived ^{36}Ar production during fission-neutron irradiation and its effect on $^{40}Ar/^{39}Ar$ ages. *Geochimica et Cosmochimica Acta*, *357*, 26–34. https://doi.org/10.1016/j.gca.2023.07.017

Cherniak, D. J. (2019). Diffusion of helium in radiation-damaged zircon. *Chemical Geology*, *529*, 119308. https://doi.org/10.1016/j.chemgeo.2019.119308

Cherniak, D. J., Watson, E. B., & Thomas, J. B. (2009). Diffusion of helium in zircon and apatite. *Chemical Geology*, *268*(1–2), 155–166. https://doi.org/10.1016/j.chemgeo.2009.08.011

Colleps, C. L., McKenzie, N. R., Guenthner, W. R., Sharma, M., Gibson, T. M., & Stockli, D. F. (2021). Apatite (U-Th)/He thermochronometric constraints on the northern extent of the Deccan large igneous province. *Earth and Planetary Science Letters*, *571*, 117087. https://doi.org/10.1016/j.epsl.2021.117087

Colleps, C. L., Mckenzie, N. R., van der Beek, P., Guenthner, W. R., Sharma, M., Nordsvan, A. R., & Stockli, D. F. (2022). Assessing the long-term low-temperature thermal evolution of the central Indian Bundelkhand Craton with a complex apatite and zircon (U-Th)/He dataset. *American Journal of Science*, *322*(10), 1089–1123. https://doi.org/10.2475/10.2022.01

Colleps, C. L., van der Beek, P., Amalberti, J., Denker, A., Tremblay, M., Bernard, M., et al. (2024). Improving the accessibility and efficiency of proton irradiations for $^{4}He/^{3}He$ thermochronology [Dataset]. Zenodo. https://doi.org/10.5281/zenodo.10532069

Cuffey, K. M., Tripathy-Lang, A., Fox, M., Stock, G. M., & Shuster, D. L. (2022). Late Cenozoic deepening of Yosemite Valley, USA. *GSA Bulletin*, *135*(5–6), 1547–1565. https://doi.org/10.1130/b36497.1

Dai, J. G., Fox, M., Han, X., Tremblay, M. M., Xu, S. Y., Shuster, D. L., et al. (2021). Two stages of accelerated exhumation in the middle reach of the Yarlung river, southern Tibet since the mid-Miocene. *Tectonics*, *40*(6), e2020TC006618. https://doi.org/10.1029/2020tc006618

Dodson, M. H. (1973). Closure temperature in cooling geochronological and petrological systems. *Contributions to Mineralogy and Petrology*, *40*(3), 259–274. https://doi.org/10.1007/bf00373790

Dygert, N., Jackson, C. R. M., Hesse, M. A., Tremblay, M. M., Shuster, D. L., & Gu, J. T. (2018). Plate tectonic cycling modulates Earth's $^{3}He/^{22}Ne$ ratio. *Earth and Planetary Science Letters*, *498*, 309–321. https://doi.org/10.1016/j.epsl.2018.06.044

Farley, K. A. (2002). (U-Th)/He dating: Techniques, calibrations, and applications. *Noble Gases in Geochemistry and Cosmochemistry*, *47*(1), 819–844. https://doi.org/10.2138/rmg.2002.47.18

Farley, K. A., Shuster, D. L., Watson, E. B., Wanser, K. H., & Balco, G. (2010). Numerical investigations of apatite $^{4}He/^{3}He$ thermochronometry. *Geochemistry, Geophysics, Geosystems*, *11*(10), Q10001. https://doi.org/10.1029/2010gc003243

Fechtig, H., & Kalbitzer, S. (1966). The diffusion of argon in potassium-bearing solids. In *Potassium argon dating*. Springer. https://doi.org/10.1007/978-3-642-87895-4_4

Flowers, R. M., & Farley, K. A. (2012). Apatite $^{4}He/^{3}He$ and (U-Th)/He evidence for an ancient grand canyon. *Science*, *338*(6114), 1616–1619. https://doi.org/10.1126/science.1229390

Flowers, R. M., Ketcham, R. A., Shuster, D. L., & Farley, K. A. (2009). Apatite (U-Th)/He thermochronometry using a radiation damage accumulation and annealing model. *Geochimica et Cosmochimica Acta*, *73*(8), 2347–2365. https://doi.org/10.1016/j.gca.2009.01.015

Flowers, R. M., Macdonald, F. A., Siddoway, C. S., & Havranek, R. (2020). Diachronous development of great unconformities before neoproterozoic snowball Earth. *Proceedings of the National Academy of Sciences of the United States of America*, *117*(19), 10172–10180. https://doi.org/10.1073/pnas.1913131117

Foland, K. A., Hubacher, F. A., & Arehart, G. B. (1992). $^{40}Ar^{39}Ar$ dating of very fine-grained samples: An encapsulated-vial procedure to overcome the problem of ^{39}Ar recoil loss. *Chemical Geology*, *102*(1–4), 269–276. https://doi.org/10.1016/0009-2541(92)90161-w

Fox, M., McKeon, R. E., & Shuster, D. L. (2014). Incorporating 3-D parent nuclide zonation for apatite $^{4}He/^{3}He$ thermochronometry: An example from the A Palachian mountains. *Geochemistry, Geophysics, Geosystems*, *15*(11), 4217–4229. https://doi.org/10.1002/2014gc005464

Gautheron, C., Tassan-Got, L., Barbarand, J., & Pagel, M. (2009). Effect of alpha-damage annealing on apatite (U-Th)/He thermochronology. *Chemical Geology*, *266*(3–4), 157–170. https://doi.org/10.1016/j.chemgeo.2009.06.001

Guenthner, W. R., Reiners, P. W., Ketcham, R. A., Nasdala, L., & Giester, G. (2013). Helium diffusion in natural zircon: Radiation damage, anisotropy, and the interpretation of zircon (U-Th)/He thermochronology. *American Journal of Science*, *313*(3), 145–198. https://doi.org/10.2475/03.2013.01

Guo, H. C., Zeitler, P. K., Idleman, B. D., Fayon, A. K., Fitzgerald, P. G., & McDannell, K. T. (2021). Helium diffusion systematics inferred from continuous ramped heating analysis of transantarctic mountains apatites showing age overdispersion. *Geochimica et Cosmochimica Acta*, *310*, 113–130. https://doi.org/10.1016/j.gca.2021.07.015

Hall, C. M. (2013). Direct measurement of recoil effects on $^{40}Ar/^{39}Ar$ standards. *Geological Society, London, Special Publications*, *378*(1), 53–62. https://doi.org/10.1144/sp378.7

Huneke, J., & Smith, S. (1976). The realities of recoil: ^{39}Ar recoil out of small grains and anomalous age patterns in ^{39}Ar-^{40}Ar dating. In *Proceedings in: Lunar science conference, 7th* (Vol. 2, pp. 1987–2008). Pergamon Press, Inc.

Iwamoto, Y., Hashimoto, S., Sato, T., Matsuda, N., Kunieda, S., Çelik, Y., et al. (2022). Benchmark study of particle and heavy-ion transport code system using shielding integral benchmark archive and database for accelerator-shielding experiments. *Journal of Nuclear Science and Technology*, *59*(5), 665–675. https://doi.org/10.1080/00223131.2021.1993372

Iwamoto, Y., Niita, K., Sawai, T., Ronningen, R. M., & Baumann, T. (2012). Improvement of radiation damage calculation in PHITS and tests for copper and tungsten irradiated with protons and heavy-ions over a wide energy range. *Nuclear Instruments & Methods in Physics Research Section B-Beam Interactions with Materials and Atoms*, *274*, 57–64. https://doi.org/10.1016/j.nimb.2011.11.038

Jourdan, F., Matzel, J. P., & Renne, P. R. (2007). ^{39}Ar and ^{37}Ar recoil loss during neutron irradiation of sanidine and plagioclase. *Geochimica et Cosmochimica Acta*, *71*(11), 2791–2808. https://doi.org/10.1016/j.gca.2007.03.017

Leya, I., Busemann, H., Baur, H., Wieler, R., Gloris, M., Neumann, S., et al. (1998). Cross sections for the proton-induced production of He and Ne isotopes from magnesium, aluminum, and silicon. *Nuclear Instruments & Methods in Physics Research Section B-Beam Interactions with Materials and Atoms*, *145*(3), 449–458. https://doi.org/10.1016/s0168-583x(98)00528-x

MacDonald, R. (1970). The ejection of atomic particles from ion bombarded solids. *Advances in Physics*, *19*(80), 457–524. https://doi.org/10.1080/00018737000101161

McDannell, K. T., Keller, C. B., Guenthner, W. R., Zeitler, P. K., & Shuster, D. L. (2022). Thermochronologic constraints on the origin of the great unconformity. *Proceedings of the National Academy of Sciences of the United States of America*, *119*(5), e2118682119. https://doi.org/10.1073/pnas.2118682119

McDannell, K. T., Zeitler, P. K., Janes, D. G., Idleman, B. D., & Fayon, A. K. (2018). Screening apatites for (U-Th)/He thermochronometry via continuous ramped heating: He age components and implications for age dispersion. *Geochimica et Cosmochimica Acta*, *223*, 90–106. https://doi.org/10.1016/j.gca.2017.11.031

Paton, C., Woodhead, J. D., Hellstrom, J. C., Hergt, J. M., Greig, A., & Maas, R. (2010). Improved laser ablation U-Pb zircon geochronology through robust downhole fractionation correction. *Geochemistry, Geophysics, Geosystems*, *11*(3), Q0AA06. https://doi.org/10.1029/2009gc002618

Reiners, P. W., Farley, K. A., & Hickes, H. J. (2002). He diffusion and (U-Th)/He thermochronometry of zircon: Initial results from fish canyon Tuff and gold butte. *Tectonophysics*, *349*(1–4), 297–308. https://doi.org/10.1016/s0040-1951(02)00058-6

Rutte, D., Pfander, J. A., Koleska, M., Jonckheere, R., & Unterricker, S. (2015). Radial fast-neutron fluence gradients during rotating ^{40}Ar/^{39}Ar sample irradiation recorded with metallic fluence monitors and geological age standards. *Geochemistry, Geophysics, Geosystems*, *16*(1), 336–345. https://doi.org/10.1002/2014gc005611

Sato, T., Iwamoto, Y., Hashimoto, S., Ogawa, T., Furuta, T., Abe, S., et al. (2018). Features of particle and heavy ion transport code system (PHITS) version 3.02. *Journal of Nuclear Science and Technology*, *55*(6), 684–690. https://doi.org/10.1080/00223131.2017.1419890

Schaeffer, O., Zähringer, J., Fechtig, H., & Kalbitzer, S. (1966). The diffusion of argon in potassium-bearing solids: Potassium argon dating (pp. 68–107).

Shuster, D. L., Cuffey, K. M., Sanders, J. W., & Balco, G. (2011). Thermochronometry reveals headward propagation of erosion in an alpine landscape. *Science*, *332*(6025), 84–88. https://doi.org/10.1126/science.1198401

Shuster, D. L., Ehlers, T. A., Rusmoren, M. E., & Farley, K. A. (2005). Rapid glacial erosion at 1.8 Ma revealed by ^{4}He/^{3}He thermochronometry. *Science*, *310*(5754), 1668–1670. https://doi.org/10.1126/science.1118519

Shuster, D. L., & Farley, K. A. (2004). ^{4}He/^{3}He thermochronometry. *Earth and Planetary Science Letters*, *217*(1–2), 1–17. https://doi.org/10.1016/s0012-821x(03)00595-8

Shuster, D. L., & Farley, K. A. (2005). Diffusion kinetics of proton-induced ^{21}Ne, ^{3}He, and ^{4}He in quartz. *Geochimica et Cosmochimica Acta*, *69*(9), 2349–2359. https://doi.org/10.1016/j.gca.2004.11.002

Shuster, D. L., Farley, K. A., Sisterson, J. M., & Burnett, D. S. (2004). Quantifying the diffusion kinetics and spatial distributions of radiogenic ^{4}He in minerals containing proton-induced ^{3}He. *Earth and Planetary Science Letters*, *217*(1–2), 19–32. https://doi.org/10.1016/s0012-821x(03)00594-6

Shuster, D. L., Flowers, R. M., & Farley, K. A. (2006). The influence of natural radiation damage on helium diffusion kinetics in apatite. *Earth and Planetary Science Letters*, *249*(3–4), 148–161. https://doi.org/10.1016/j.epsl.2006.07.028

Tremblay, M. M., Fox, M., Schmidt, J. L., Tripathy-Lang, A., Wielicki, M. M., Harrison, T. M., et al. (2015). Erosion in southern Tibet shut down at approximately 10 Ma due to enhanced rock uplift within the Himalaya. *Proceedings of the National Academy of Sciences of the United States of America*, *112*(39), 12030–12035. https://doi.org/10.1073/pnas.1515652112

Tremblay, M. M., Shuster, D. L., & Balco, G. (2014). Diffusion kinetics of ^{3}He and ^{21}Ne in quartz and implications for cosmogenic noble gas paleothermometry. *Geochimica et Cosmochimica Acta*, *142*, 186–204. https://doi.org/10.1016/j.gca.2014.08.010

Tripathy-Lang, A., Fox, M., & Shuster, D. L. (2015). Zircon ^{4}He/^{3}He thermochronometry. *Geochimica et Cosmochimica Acta*, *166*, 1–14. https://doi.org/10.1016/j.gca.2015.05.027

Valla, P. G., Shuster, D. L., & van der Beek, P. A. (2011). Significant increase in relief of the European Alps during mid-Pleistocene glaciations. *Nature Geoscience*, *4*(10), 688–692. https://doi.org/10.1038/ngeo1242

Valla, P. G., van der Beek, P. A., Shuster, D. L., Braun, J., Herman, F., Tassan-Got, L., & Gautheron, C. (2012). Late Neogene exhumation and relief development of the Aar and Aiguilles Rouges massifs (Swiss Alps) from low-temperature thermochronology modeling and ^{4}He/^{3}He thermochronometry. *Journal of Geophysical Research*, *117*(F1), F01004. https://doi.org/10.1029/2011jf002043

Vermeesch, P., Tian, Y., Schwanethal, J., & Buret, Y. (2023). Technical note: In situ U–Th–He dating by ^{4}He/^{3}He laser microprobe analysis. *Geochronology Discuss*, *2023*(2), 1–15. https://doi.org/10.5194/gchron-5-323-2023

Zeitler, P. K., Herczeg, A. L., Mcdougall, I., & Honda, M. (1987). U-Th-He dating of apatite - A potential thermochronometer. *Geochimica et Cosmochimica Acta*, *51*(10), 2865–2868. https://doi.org/10.1016/0016-7037(87)90164-5

Ziegler, J. F., Ziegler, M. D., & Biersack, J. P. (2010). SRIM - The stopping and range of ions in matter (2010). *Nuclear Instruments & Methods in Physics Research Section B-Beam Interactions with Materials and Atoms*, *268*(11–12), 1818–1823. https://doi.org/10.1016/j.nimb.2010.02.091